REVIEW
Editor's Choice
small methods
www.small-methods.com

Advances in Axial Resolution Strategies for Super-Resolution Imaging Systems

Qiwen Tan, Hongjun Wu, Yongtao Liu, Qian Chen,* and Chao Zuo**

3D fluorescence super-resolution imaging technology can reconstruct the 3D structure of biological cells in space, which is crucial for observing the intricate internal structures of cells and studying the organization and function of tissues and organs. However, even with super-resolution imaging techniques that surpass the diffraction limit, the axial resolution typically only reaches one-third to one-half of the lateral resolution. Achieving true axial or 3D super-resolution imaging of samples remains a significant challenge. In light of this, this review summarizes the research progress in axial super-resolution imaging techniques, with a focus on the principles, developments, and characteristics of these techniques, and provides an outlook on their future development directions. This paper aims to provide valuable reference material for researchers in the field.

1. Introduction

As early as 1873, the German scientist Abbe[1] proposed the Abbe optical diffraction limit theory, which states that the resolution of optical microscopes cannot be infinitely improved but instead has a theoretical upper limit, known as the Abbe diffraction limit. The reason for this resolution limit can be understood as the spatial spectrum on the frequency plane (the back focal plane of the objective) being restricted to a finite range due to the inherently limited aperture of the optical system. The highest spatial frequency that can pass through this finite range is referred to as the cutoff frequency of the optical system, and its reciprocal corresponds to the system's limit resolution. This lateral and axial resolution can be expressed as:

$$d_{xy} = \frac{\lambda}{2NA}, \quad d_z = \frac{2\lambda}{NA^2} \tag{1}$$

where λ is the wavelength of light and NA is the numerical aperture of the microscope objective. Due to the existence of this diffraction limit, traditional optical microscopes are cannot to surpass the resolution restriction imposed by diffraction, preventing higher-resolution imaging of fine structures and cellular organelles.[2] In response, scientists have made numerous efforts, employing a range of physical or chemical methods to overcome this diffraction limit, leading to the emergence of super-resolution imaging techniques, which have become a new frontier in the development of optical microscopy.[3] Among these, fluorescence-based super-resolution imaging technologies, which rely on chemical methods, have experienced rapid advancement due to their excellent practical applications. In 2014, the Nobel Prize in Chemistry was awarded to three scientists—Eric Betzig, Stefan Hell, and William Moerner—for their significant contributions to the field of fluorescence super-resolution imaging: Betzig for the invention of single-molecule localization microscopy (SMLM), Hell for stimulated emission depletion microscopy (STED), and Moerner for the discovery of the fluorescence protein photoactivation effect.[4] This recognition marked the entry of fluorescence microscopy into the "nanometer era". Among these, single-molecule localization-based methods differ from traditional fluorescence super-resolution techniques in that they do not directly improve the optical resolution in the conventional sense. Instead, they reconstruct super-resolution images of the sample based on highly precise single-molecule localization. The effective spatial resolution achieved is typically characterized by the localization precision, which refers to the distribution of measured fluorescence emitter positions around their mean value when measured multiple times. For 2D Gaussian fitting, the localization precision can be simply expressed as:[5]

$$\sigma \geq \frac{\sigma_{PSF}}{\sqrt{N}} \tag{2}$$

where σ_{PSF} is the standard deviation corresponding to the PSF distribution and N is the total number of photons collected. It can be seen that the more the number of collected photons, the higher the precision of localization.

With the passage of time, super-resolution imaging technology has undergone continuous innovation and improvement. Several super-resolution far-field microscopy techniques have achieved a lateral imaging resolution of ≈20–50 nm;[6] In contrast to

Q. Tan, H. Wu, Y. Liu, C. Zuo
Smart Computational Imaging Laboratory (SCILab), School of Electronic and Optical Engineering
Nanjing University of Science and Technology
Nanjing, Jiangsu Province 210094, China
E-mail: Yongtao.Liu@njust.edu.cn; zuochao@njust.edu.cn

Q. Tan, H. Wu, Y. Liu, Q. Chen, C. Zuo
Jiangsu Key Laboratory of Spectral Imaging & Intelligent Sense
Nanjing University of Science and Technology
Nanjing, Jiangsu Province 210094, China
E-mail: chenqian@njust.edu.cn

Q. Tan, H. Wu, Y. Liu, C. Zuo
Smart Computational Imaging Research Institute (SCIRI) of Nanjing University of Science and Technology
Nanjing, Jiangsu Province 210094, China

The ORCID identification number(s) for the author(s) of this article can be found under https://doi.org/10.1002/smtd.202401926

DOI: 10.1002/smtd.202401926

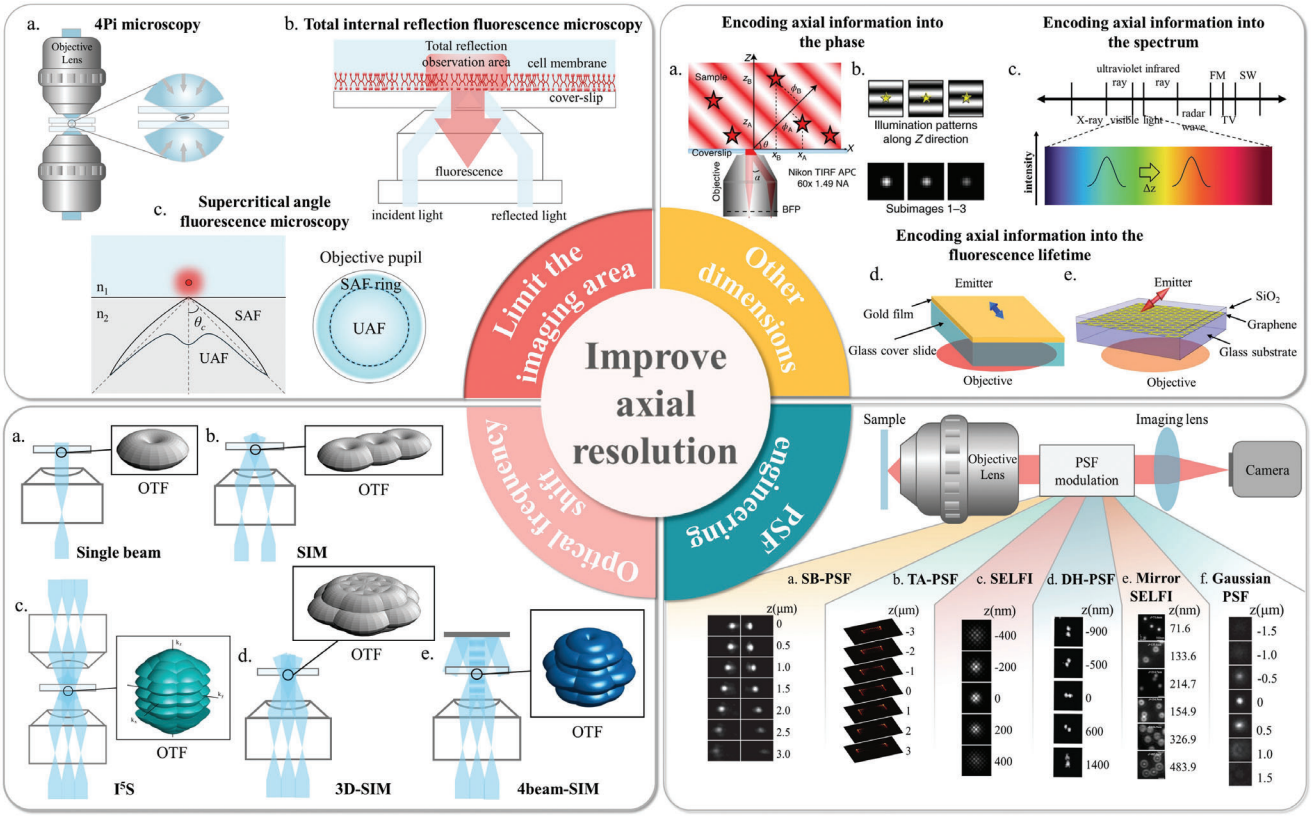

Figure 1. Summary frame diagram of axial super resolution imaging technology.[13] Reproduced (Adapted) with permission.[13h] Copyright 2008, Publisher Elsevier. Reproduced (Adapted) with permission.[13c] Copyright 2008, Elsevier. Reproduced (Adapted) with permission.[13i] Copyright 2023, Authors. Reproduced (Adapted) with permission.[13d] Copyright 2014, Springer Nature. Reproduced (Adapted) with permission.[13j] Copyright 2009, National Academy of Sciences. Reproduced (Adapted) with permission.[13k] Copyright 2020, American Physical Society. Reproduced (Adapted) with permission.[13g] Copyright 2018, Springer Nature. Reproduced (Adapted) with permission.[13a] Copyright 2021, Springer Nature. Reproduced (Adapted) with permission.[13e] Copyright 2021, Springer Nature. Reproduced (Adapted) with permission.[13f] Copyright 2021, Springer Nature. Reproduced (Adapted) with permission.[13b] Copyright 2019, Springer Nature.

lateral super-resolution imaging techniques, research on breaking the diffraction limit of axial resolution has been relatively limited. However, improving axial resolution is of significant importance for applications such as studying the 3D organization of samples, enhancing the accuracy of single-molecule localization and tracking, and observing details of thick samples and deep tissues. Traditional 3D fluorescence imaging typically employs confocal microscopy or multiphoton microscopy. Confocal laser scanning microscopy reduces the effects of defocus using a pair of confocal pinholes, providing good optical sectioning and 3D imaging capabilities.[7] Multiphoton laser scanning microscopy, based on the multi-photon absorption theory, generates multi-photon excitation in a small region near the focal point, offering inherent 3D imaging capabilities.[8] However, neither of these techniques results in significant improvements in axial resolution.[4e,9] Furthermore, with the development of sample clearing techniques,[10] light-sheet fluorescence microscopy (LSFM) has achieved excellent 3D imaging capabilities, and it has fast imaging speeds, making it more suitable for observing dynamic samples. However, the spatial resolution of this technique is typically at the micrometer scale, and the axial resolution is generally lower than the lateral resolution.[11] In summary, due to limitations such as diffraction of light, axial undersampling, and optical aberrations, even in super-resolution imaging techniques that surpass the diffraction limit, the axial resolution in current 3D fluorescence imaging technologies is typically only 1/3 to 1/2 of the lateral resolution, making isotropic resolution difficult to achieve.[12]

This paper provides a comprehensive review of the research progress in axial super-resolution imaging technologies. Based on the principles of different techniques, the methods are categorized into four types: Localized Excitation, Optical Frequency Shift, Point Spread Function (PSF) Engineering and Encoding Axial Information into Alternative Dimensions (**Figure 1**). The principles of various axial super-resolution techniques are discussed in detail, and the resolution, imaging speed, imaging depth, system complexity, and other characteristics of different techniques are compared and analyzed. Finally, we conclude the paper and provide references for the further development and wide application of these technologies.

2. Axial Resolution Enhancement Based on Localized Excitation

This chapter primarily introduces three methods for enhancing axial resolution through restricted imaging volumes, including

4Pi super-resolution microscopy based on opposing objective lens illumination interference, total internal reflection fluorescence microscopy and supercritical angle fluorescence microscopy based on evanescent waves. It reviews various axial super-resolution imaging techniques based on this principle, with a focus on the latest technological advancements in this field.

2.1. 4Pi Super-Resolution Microscopy

According to the Rayleigh criterion, the size of the PSF can be reduced by increasing the receiving angle of the objective lens to improve the resolution of the system.[14] In 1992, Hell et al.[15] designed and experimentally validated a 4Pi super-resolution microscope based on two opposing objective lenses. Each objective lens covers only a half-aperture angle of ≈65°, and the use of two objective lenses can almost completely cover the entire 4π solid angle, allowing for the generation of a nearly complete spherical wavefront, and the shape of the system PSF is basically maintained as a sphere, enabling 3D isotropic resolution.[15,16] 4Pi microscopy can be divided into A-type, B-type and C-type 4Pi architectures by different ways of interference PSF formation.[17] The PSF of the A-type 4Pi architecture is generated by focusing two beams of backward-propagating coherent excitation light on the confocal plane through two opposite objective lenses. The B-type 4Pi architecture interferes on the detector by collecting the fluorescence signal in the opposite direction of the objective lens. The A-type and B-type 4Pi architectures can increase the axial resolution by three to four times. The C-type 4Pi architecture simultaneously makes the excitation light and the fluorescence coherent, which can improve the axial resolution by about seven times (**Figure 2a**).

By combining it with other super-resolution microscopy techniques, 4Pi microscopy can significantly enhance the axial resolution of certain super-resolution systems. In 2008, Schmidt et al.[19] proposed isoSTED, which was combined with STED to obtain an isotropic 3D resolution super-resolution microscope with 3D localization precision reaching ≈40–50 nm. In 2009, Shtengel et al.[20] proposed interferometric light-activated localization microscopy (iPALM), which combines PALM with 4Pi microscopy. iPALM uses three channels with a phase difference of $\pi/3$ for axial localization and achieves 3D localization with a precision of up to 20 nm through centroid fitting for lateral localization. However, it suffers from the limitation of shallow imaging depth. In 2011, Hell's group[21] experimentally realized the combination of 4Pi microscopy with SMLM, that is, the 4Pi-SMS technique. 4Pi-SMS utilizes achromatic quarter-wave slices and a modified Babinet-Soleil compensator to achieve time-separated fluorescent wave packets that are imaged in the different quadrants of a single EMCCD. This greatly improves localization accuracy (Figure 2b). Compared to iPALM, 4Pi-SMS has a deeper imaging depth of up to 1000 nm, and it has a 3D localization precision of 10 nm or even less in layers up to 650 nm thick. The 4Pi-SMS combines multi-color recording, nanoscale resolution, and extended axial depth, greatly advancing non-invasive 3D imaging of cells and other transparent materials. In 2016, in order to solve the problem of rapid deterioration of resolution on thick samples by microscopy techniques such as 4Pi-SMS and to further extend the imaging depth, Huang et al.[22] introduce a whole-cell 4Pi single-molecule switching nanoscopy (W-4PiSMSN); W-4PiSMSN optimizes PSF quality in thick samples by introducing deformable mirrors and improves axial localization accuracy by combining the interferometric phase and centrifugal rate of PSFs. The technique achieves a 3D localization precision of 10–20 nm over the full thickness of mammalian cells, and its imaging depth can reach about 10 μm.

Notably, in 2022, Bates et al.[18] reported a 4Pi-STORM microscopy, which combines 4Pi microscopy with STORM super-resolution microscopy to improve axial localization precision (≈2–3 nm) and maintains high-precision near-isotropic 3D resolution over larger imaging depths by modeling a dynamic spline PSF for the 4Pi PSF. The microscopy optical path diagram is shown in Figure 2c, in which the interferometric phase of a single molecule can be determined by acquiring the intensity of the same fluorescent molecule in the four channels. In order to overcome the interference modulation phase shift with time caused by disturbance in optical cavity (Figure 2d), they implemented a method for measuring PSF phase by numerical moving experiment (Figure 2e), measured the time-dependent phase of detecting PSF from positioning data (Figure 2f) and obtained the complete time evolution process of PSF phase during acquisition (Figure 2g). This model is the dynamic spline PSF model. Compared to the previous method, this method overcomes the problem that the image quality deteriorates with increasing depth and achieves higher positioning accuracy and lower artifact rate. However, while the 4Pi-based super-resolution microscopy method has achieved extremely high 3D localization accuracy over a large area, its complex optical setup and the need for extensive maintenance make it difficult to be implemented as a commercial product for broader biological applications.

2.2. Total Internal Reflection Fluorescence Microscopy

When light undergoes total internal reflection at an interface with an incidence angle greater than the critical angle, no refracted light is generated (**Figure 3a**). However, the evanescent wave emitted by fluorescent molecules can propagate through the interface, with its intensity exponentially decaying as the distance increases. This allows for the excitation of fluorescent labels in the surface-near region (50–200 nm), eliminating background signals from deeper layers and enabling high-sensitivity, high-contrast fluorescence imaging of ultra-thin surface layers.

Using the evanescent illumination field of total internal reflection to obtain sub-diffraction axial information in optical microscopy dates back to the 1950s.[23] In the late 1970s, Lanni et al.[23b,24] first obtained axial position from the photometric readings of 3T3 fibroblasts irradiated by total internal reflection fluorescence at two different incident angles, and theoretically calibrated it based on the Lukosz model. In the early 1980s, Axelrod[25] introduced total internal reflection fluorescence microscopy (TIRFM) and demonstrated various applications, including obtaining sub-diffraction axial resolution by analyzing the variation of TIRF intensity with incident angle. It was not until the end of the 20th century that TIRF became widely used, following advancements in laser technology, objective lens, and ultra-sensitive detectors.[26] In 2021, Szalai and Siarry[27]

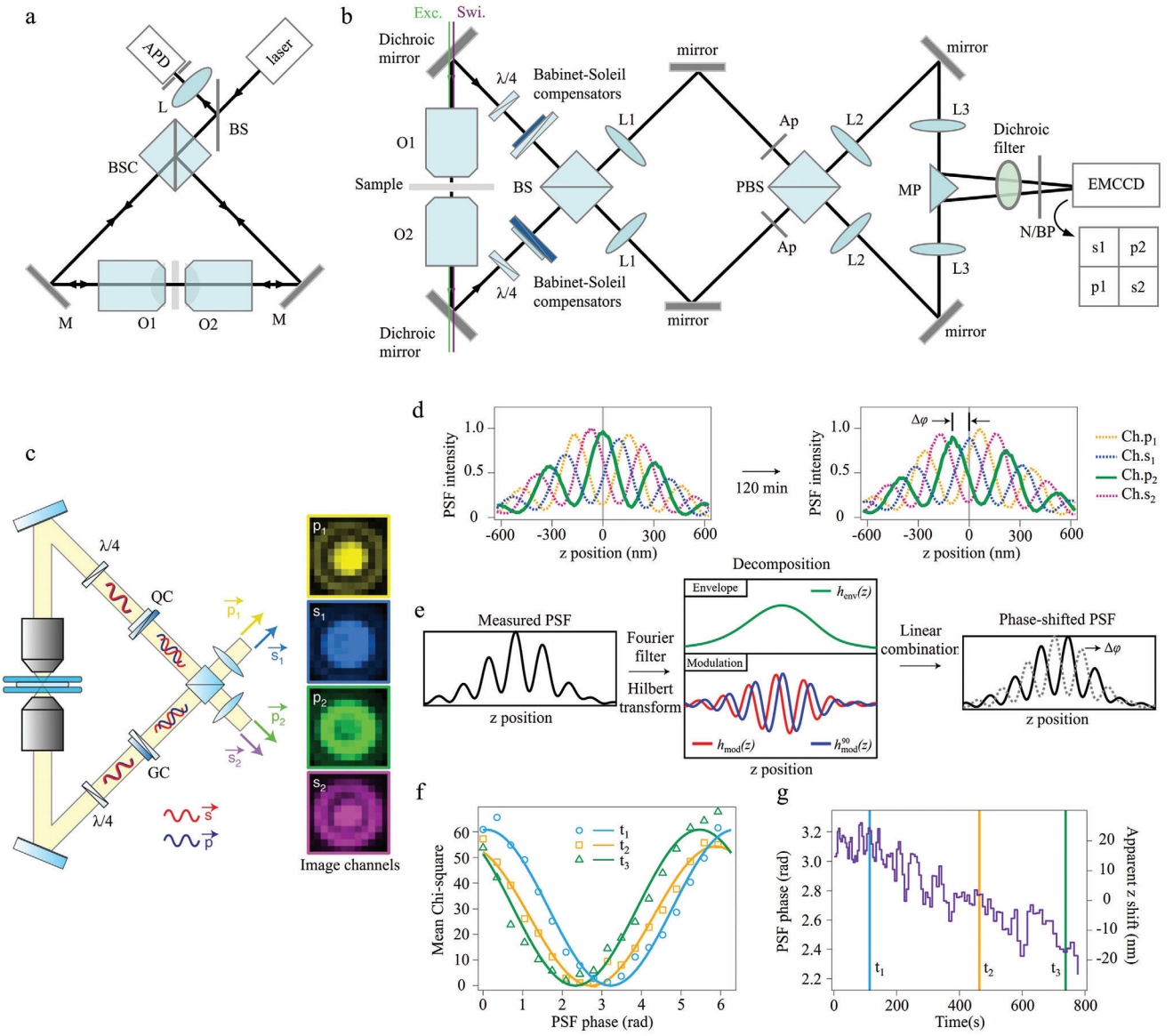

Figure 2. a) Sketch of the optical path of the C-type 4Pi architecture. b) Sketch of the optical path of the 4Pi-SMS. c) Schematic of the 4Pi-STORM optical path.[18] d) Shift of the center profile of the 4Pi PSF with respect to the focal plane modulation phase.[18] e) Graphical representation of the phase shift transformation.[18] f) Measurement of the PSF phase. g) Evolution of the PSF phase over time.[18] Reproduced (Adapted) with permission.[18] Copyright 2022, Authors.

proposed a photometric method (SIMPLER) for decoding the axial position of a single molecule using 3D total internal reflection fluorescence nanoscopy. This method combines DNA-PAINT[28] and dSTORM to achieve axial localization precision of less than 10 and 20 nm in the axial range of 250 nm, respectively.

SIMPLER decodes the axial position of a single molecule based on three phenomena: the axial dependence of the excitation intensity, the axial dependence of the fluorescence angular emission, and the axially independent transverse PSF of the single molecule signal on the image plane (Figure 3c). By combining these three phenomena, the relationship between the fluorescence signal and the axial position is derived, which forms the core of SIMPLER axial localization. In the context of SMLM, the fluorescence signal can be represented as the number of the number of photons, N, detected during the camera frame acquisition time and normalized by the number of photons N_0 at $z = 0$. The expression for the experimentally estimated axial position obtained in this way is:

$$\hat{z} = d_F \times \ln\left(\alpha_F / \left(N/N_0 - \left(1 - \alpha_F\right)\right)\right) \tag{3}$$

where 1-α is the scattering contribution fraction, and d_F is the penetration depth. From this, it can be concluded that SIMPLER can directly decode axial information from 2D SMLM data, making it fully compatible with any 2D SMLM system. It does not require any hardware modifications to

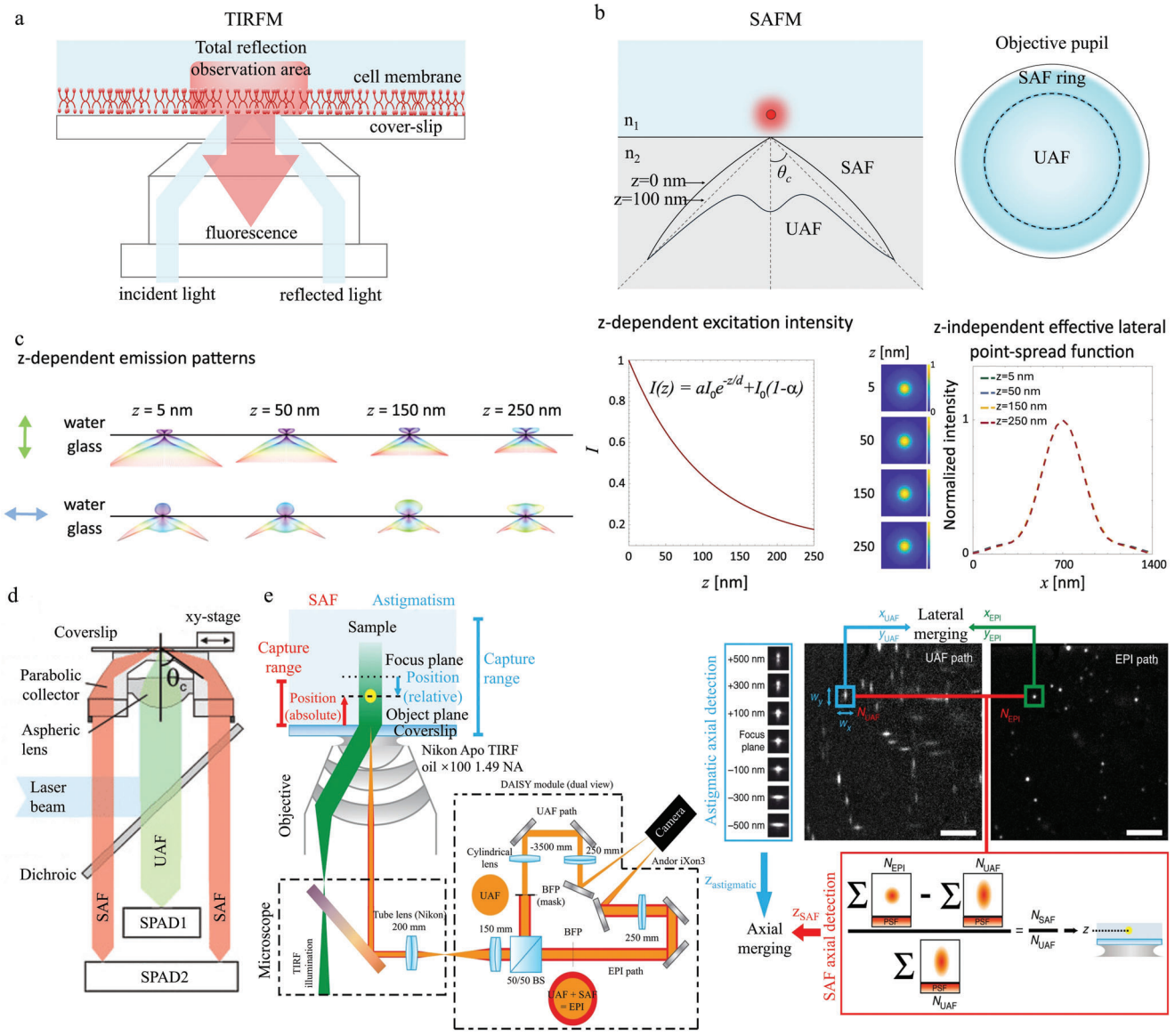

Figure 3. a) Schematic diagram of the principle of TIRFM. b) Schematic diagram of the principle of SAFM. c) SIMPLER decodes the axial position of a single molecule based on three phenomena.[27] Reproduced (Adapted) with permission.[27] Copyright 2022, Springer Nature. d) Schematic diagram of 3D-SAFM optical path.[29] Reproduced (Adapted) with permission.[29] Copyright 2008, American Physical Society. e) Schematic of DAISY 's experimental setup and data analysis.[30] Reproduced (Adapted) with permission.[30] Copyright 2019, Springer Nature.

wide-field single-molecule fluorescence microscopes, demonstrating strong robustness, and can achieve nanometer-level resolution without the need for drift correction.

2.3. Supercritical Angle Fluorescence Microscopy

Supercritical Angle Fluorescence Microscopy (SAFM) is also a fluorescence microscopy technique based on total internal reflection, which represents an innovation on traditional TIRFM. This method overcomes the limitations of high-angle illumination and the difficulty of forming sub-micron focal spots in TIRFM, providing a new approach for studying surface-bound reactions. Supercritical Angle Fluorescence (SAF) refers to fluorescence transmitted at the interface at an angle greater than the critical angle. In contrast, Ultra-Angular Fluorescence (UAF) refers to fluorescence transmitted at the interface at an angle less than the critical angle (Figure 3b).[31]

In 2004, Ruckstuhl and Verdes[32] first proposed SAFM. The special feature of SAFM is the separation and collection of two different fluorescence emission modes. One of the light paths covers the fluorescence entering the glass at a low surface angle, and the other captures the fluorescence at a high angle: beyond the critical angle of the water/glass interface. Due to the collection of SAF, the volume of confocal detection is strictly limited to the interface, while UAF collects deeper information from aqueous solution. Therefore, the system can simultaneously transmit the information of the surface binding and non-binding parts

of the fluorescent analyte.[33] Based on this, in 2010, they[29] invented the 3D Supercritical Angle Fluorescence Microscope (3D-SAFM), which improved the axial resolution to the nanometer scale and enhanced the 3D imaging capability. Unlike previous methods, the axial position in this approach is determined by measuring the ratio of SAF to UAF, which extends the axial localization range (Figure 3d). 3D-SAFM can achieve axial localization accuracy of up to 15 nm and can be combined with super-resolution techniques such as STED, offering a certain degree of versatility. In 2014, Deschamps et al.[33b] established a robust and simple single-molecule localization microscopic supercritical angle fluorescence detection method. This method obtains the ratio of epifluorescence (EPI) and UAF through two imaging channels to obtain the absolute axial position information of a single molecule, which is called virtual supercritical angle fluorescence microscope (vSAF). This method overcomes the diffraction effects caused by mask edges in SAFM, achieving single-molecule 3D super-resolution localization while maintaining lateral resolution. By further utilizing high numerical aperture objectives to directly detect SAF, combining adaptive optics to reduce spherical aberrations, and employing a new PSF fitting model, this approach can achieve nearly isotropic 3D resolution. Then, a similar approach to vSAF proposed by Bourg et al.[34] in 2015: the Direct Optical Nanoscopy with Axial Localized Detection (DONALD), what sets this method apart is its use of TIRF excitation combined with direct stochastic optical reconstruction microscopy (dSTORM), which experimentally achieved an isotropic 3D localization precision of up to 20 nm within a 150 nm axial range. However, techniques based on TIRF generally provide good optical sectioning capabilities only very close to the sample surface. To extend the imaging depth while maintaining high localization precision, in 2019, Cabriel et al.[30] proposed Dual-view Astigmatic Imaging with SAF Yield (DAISY) by combining DONALD with astigmatism. DAISY provides 3D super-resolution imaging through dual-channel detection, with axial detection separated from lateral detection and independent of each other. DAISY provides 3D super-resolution imaging through dual-channel detection, with axial and transverse detection separated and optimized independently (Figure 3e). DAISY utilizes both SAF and astigmatic for axial localization, and EPI and UAF for transverse localization, resulting in stable 3D localization precision better than 20 nm over 600 nm, and its localization depth has been extended to the micrometer level. Correspondingly, DONALD and DAISY, by combining both TIRFM and SAFM, can achieve better performance, but at the cost of increased system complexity.

3. Axial Resolution Enhancement Based on Optical Frequency Shifting

Optical frequency-shift super-resolution imaging technology is based on the principle of synthetic aperture. By transferring the high-frequency information of the observation target which cannot be obtained by traditional optical microscopes to the low-frequency passband range, and then applying a series of subsequent spectrum demodulation methods, this technique enables the acquisition of a wider frequency band of the observation target spectral information to achieve super-resolution imaging. Compared to other techniques, optical frequency-shift super-resolution imaging technology combines the super-resolution imaging capabilities of non- fluorescent-labeled samples and fluorescent labeled samples, and offering advantages such as fast imaging speed, high sample universality, and low phototoxicity.[35] This section focuses on various optical frequency-shifted axial super-resolution imaging techniques based on structured light illumination.

The optical transfer function (OTF) describes to what extent and with what phase shift the spatial frequency k of an object is transferred to the observed image, and thus it determines the spatial frequency that can be observed by the microscope. As shown in **Figure 4a**, the optical transfer function of the traditional microscope is an annular region, and its depression near the k_z axis region is the cause of the inconsistency between the lateral and axial resolutions.[36]

In 2000, Gustafsson et al.[37] from the Howard Hughes Medical Institute confirmed the feasibility of structured illumination microscopy (SIM) for the first time, and its lateral resolution reaching ≈120–150 nm. The sinusoidal illumination mode of SIM is formed by the interference of two beams of light and contains only three Fourier components in the frequency domain; therefore, its OTF is represented by the superposition of three shift copies of the traditional optical microscope OTF (Figure 4b); the lateral resolution of the region has been significantly improved, but its depression still exists, and the axial resolution has not been significantly improved, which makes it difficult to achieve 3D reconstruction.[38]

In 2008, Gustafsson[13h] proposed 3D-SIM technology and published experimental proof, its lateral and axial resolution can reach twice the resolution of traditional optical microscopy. The 3D-SIM uses an improved illumination structure, and the fluorescent sample is illuminated by three coherent excitation lights (Figure 4c). The total intensity distribution can be regarded as the coherent superposition of plane waves with different wave vectors:

$$I(r) \propto \left|\sum_j E_j e^{ik_j\cdot r}\right|^2 = \& \left(\sum_j E_j^* e^{-jk_j\cdot r}\right)\cdot\left(\sum_q E_q e^{ik_q\cdot r}\right) = \& \left(\sum_{j,q} E_j^* \cdot E_q e^{i\left(k_q-k_j\right)\cdot r}\right) \quad (4)$$

Among them, the difference between any two plane wave propagation vectors constitutes a spatial component, so the interference between the three illumination beams produces a 3D illumination mode containing seven Fourier components; after convolution with the traditional optical microscope, this process OTF fills the lack of axial resolution. Figure 4**c** shows the OTF after using three lighting mode directions. In the actual imaging process, a few incoherent beams are often introduced into the three coherent beams to reduce the imaging artifacts and limit the interference effect to a finite axial range around the focal plane. Compared with the fully coherent case, the (OTF) generated by the incoherence of a few beams is only slightly broadened in the axial direction, and the 3D-SIM image reconstruction method of fully coherent light is still applicable. The transverse and axial resolutions of 3D-SIM have been doubled, but its axial

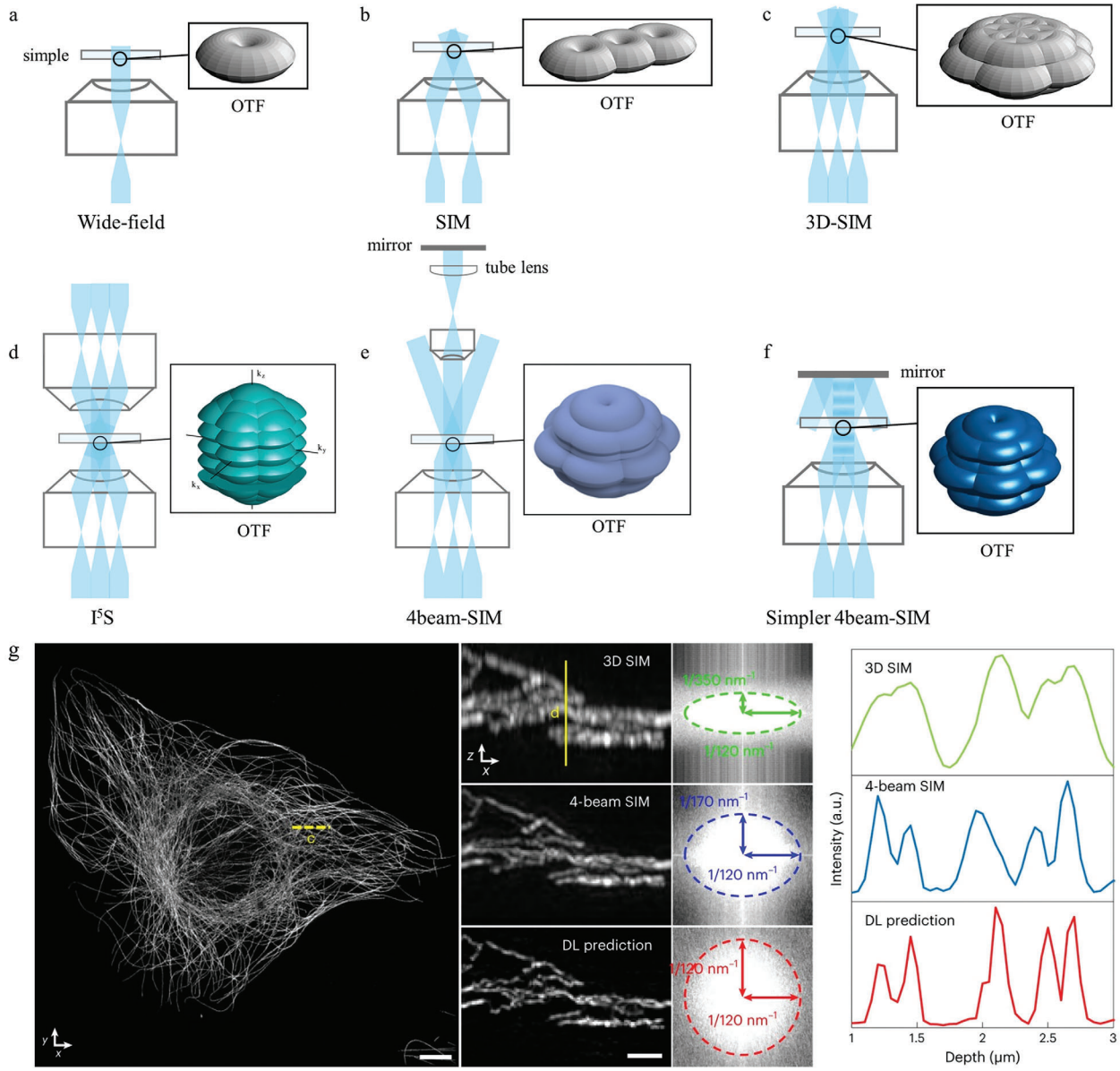

Figure 4. Axial super-resolution imaging techniques based on optical frequency shifting. a–f) Include simple schematic diagrams of the optical path and OTF for each method: a) Wide-field;[13h] Reproduced (Adapted) with permission.[13h] Copyright 2008, Elsevier. b) SIM;[13h] Reproduced (Adapted) with permission.[13h] Copyright 2008, Elsevier. c) 3D-SIM;[13h] Reproduced (Adapted) with permission.[13h] Copyright 2008, Elsevier. d) I^5S;[13c] Reproduced (Adapted) with permission.[13c] Copyright 2008, Elsevier. e) 4beam-SIM;[39] Reproduced (Adapted) with permission.[39] Copyright 2020, Optical Society of America. f) Simpler 4beam-SIM.[13i] Reproduced (Adapted) with permission.[13i] Copyright 2023, Springer Nature. g) Alexa Fluor 488-immunolabeled microtubules in a fixed U2OS cell using conventional microscopy, 4-beam SIM and deep learning prediction, and line profiles corresponding to yellow solid line.[13i] Reproduced (Adapted) with permission.[13i] Copyright 2023, Springer Nature.

resolution is still limited to 300 nm, which is much lower than its transverse resolution of 120 nm.

Similarly, in 2008, Lin Shao et al.[13c] of Gustafsson 's team proposed a wide-field microscope with a 3D resolution of 100 nm: I^5S. I^5S uses an opposing-objective configuration combined with a 3D-SIM structural illumination system, introducing six coherent light beams as shown in Figure 4d. This setup provides more frequency components than 3D-SIM, enabling an isotropic resolution of 100 nm. However, the introduction of dual objectives in I^5S also implies an increase in optical path complexity.

To further simplify the system and obtain high axial resolution, Manton[39] proposed a method that can be directly added to 3D-SIM microscope in 2020: On the conventional 3D-SIM microscope, a low numerical aperture, high working distance objective was added on the other side of the sample and the imaging of four-beam interference was generated by reflecting the central beam through the mirror, obtaining a four-beam interference pattern with a finer axial structure, which ultimately leads to a 3D image with an isotropic resolution of 125 nm (Figure 4e). Compared with I^5S, this method simplifies the complexity of the

optical system. Nevertheless, the optical path of this method is still too complicated compared with 3D-SIM, and a special laser source is needed to achieve a long interference length to meet the interference between the reflection center beam and the original three beams. In addition, as with I^5S, a slight refractive index mismatch will introduce a large number of aberrations.

Based on this, in 2023, Li et al.[13i] reported two methods to enhance the axial resolution of 3D structured light illumination microscopy, including 4-beam SIM and deep learning neural network for improving axial resolution, and verified these methods on fixed cell and living cell samples. The 4-beam SIM is based on the 3D-SIM optical path, and the mirror is immersed in the sample solution and placed directly on the opposite side of the sample, so that four-beam interference can be realized, and a higher axial spatial free frequency component can be generated in the illumination mode, as shown in Figure 4f; it can achieve an axial resolution of 160 nm and obtain almost isotropic 3D reconstruction (Figure 4g).

4-beam SIM has many advantages over I^5S and dual-objective four-beam methods, including a simplified optical path, reduced aberration, and ease of implementation. However, the 4-beam SIM technique is susceptible to phototoxicity[40] when imaging fine structures smaller than the resolution limit with occasional ringing artifacts and the large number of raw images for reconstruction require longer experimental times. In this regard, 3D-SIM requires much shorter illumination time and is more conducive to sustained 4D imaging.[41] Based on this, they simultaneously proposed a method to improve axial resolution based on deep learning, achieving an isotropic resolution of about 120 nm (Figure 4g). The advantage of this method is that the training data itself contains true values,[42] and it can be used for other 3D super-resolution imaging techniques other than 3D-SIM, such as confocal microscopy, STED, etc.

For optical frequency-shift super-resolution imaging technology, in addition to the microscopic imaging technology based on structured light illumination introduced in this paper, optical frequency-shift super-resolution imaging can also be realized by using evanescent field (NWRIM,[43] etc.) and surface plasmon (pSIM,[44] LP-SIM,[45] etc.). The resolution of spatial frequency-shift super-resolution imaging technology based on evanescent field is often only improved in the direction of evanescent wave vector, and its resolution varies in different directions. In addition, the imaging depth of the surface plasmon-based method is limited by the evanescent wave attenuation depth, but this also means that the high signal-to-noise ratio imaging results of the sample surface can be obtained.[46]

4. Axial Resolution Enhancement Based on PSF Engineering

PSF is an critical parameter for assessing the imaging performance of a microscope, with an unmodulated PSF being symmetric with respect to the focal plane. The optical path diagram for axial super-resolution localization based on PSF engineering is shown in **Figure 5a**. By deliberately introducing defocus, optical aberrations, spatial light phase masks, the PSF can be axially modulated, resulting in changes in the spatial distribution of the PSF that are related to the axial position. By extracting shape features and other parameters of the PSF, the axial position of the sample can be monitored over a wide range. This section introduces various axial super-resolution imaging techniques based on PSF engineering.

4.1. Double-Helix PSF

The human visual system uses defocus as depth information: the farther the object is from the focal plane, the more blurred it becomes. Inspired by this, the defocus depth method obtains depth information by cross-evaluating frame images taken at different focus or aperture settings.[47] However, the PSF of such systems has not been optimized for depth estimation (Figure 5b). In 2006, Greengard et al.[48] proposed a new depth estimation method based on spatial rotation PSFs. They obtained the double-helix beam by linearly superimposing the Laguerre-Gauss (LG) mode, and then obtained the Double-Helix PSF (DH-PSF), which opened the door to the research and application of DH-PSF technology.

In 2009, Pavani et al.[13j] realized 3D single-molecule fluorescence imaging beyond the optical diffraction limit using a wide-field microscope with a DH-PSF. The lateral localization accuracy is as low as 10 nm, and the axial localization accuracy is as low as 20 nm. Moreover, this method is suitable for 3D super-resolution imaging of individual fluorescent molecules in thick samples within a large depth of field (2 μm). The signal processing part is essentially a 4f imaging system, when the reflective phase-only spatial light modulator (SLM)[49] on the Fourier plane is loaded with the DH-PSF phase[50] mask, the spectral information of the sample image will be modulated by the DH-PSF transfer function. Finally, each object point will be convoluted with the DH-PSF lobes. Each molecule in the detected DH-PSF image will appear with two lobes. The lateral position of the molecule is estimated by the midpoint of the line connecting the two lobes. The axial position depends on the direction and angle of the line connecting the two lobes, when the molecule is on the focus, its DH-PSF lobe is horizontal, and when the molecule is far away from the focus, the direction of its lobe connection begins to rotate. The axial position of the molecule is estimated by creating a calibration plot of angle versus axial position (Figure 5c). Combined with photoactivatable fluorophores, DH-PSF microscopy obtained super-resolution imaging of microtubule network structures in immobilized mammalian cells over a large axial range in three dimensions.[51] However, due to the high energy loss of SLM,[13j,52] the photon utilization efficiency of this method is low. To improve localization precision, high-brightness fluorescent dyes or long exposure time are needed. Improvements in phase mask design, optimized estimator, background minimization, and closed-loop drift correction can overcome some of the shortcomings of the method and achieve further improvement in resolution.[53]

4.2. 3D Stochastic Optical Reconstruction Microscopy

In 2008, Hang et al.[54] from Zhuang's team implemented 3D Stochastic Optical Reconstruction Microscopy (3D-STORM) using optical astigmatism to determine the lateral and axial positions of individual fluorophores with nanometer precision, and

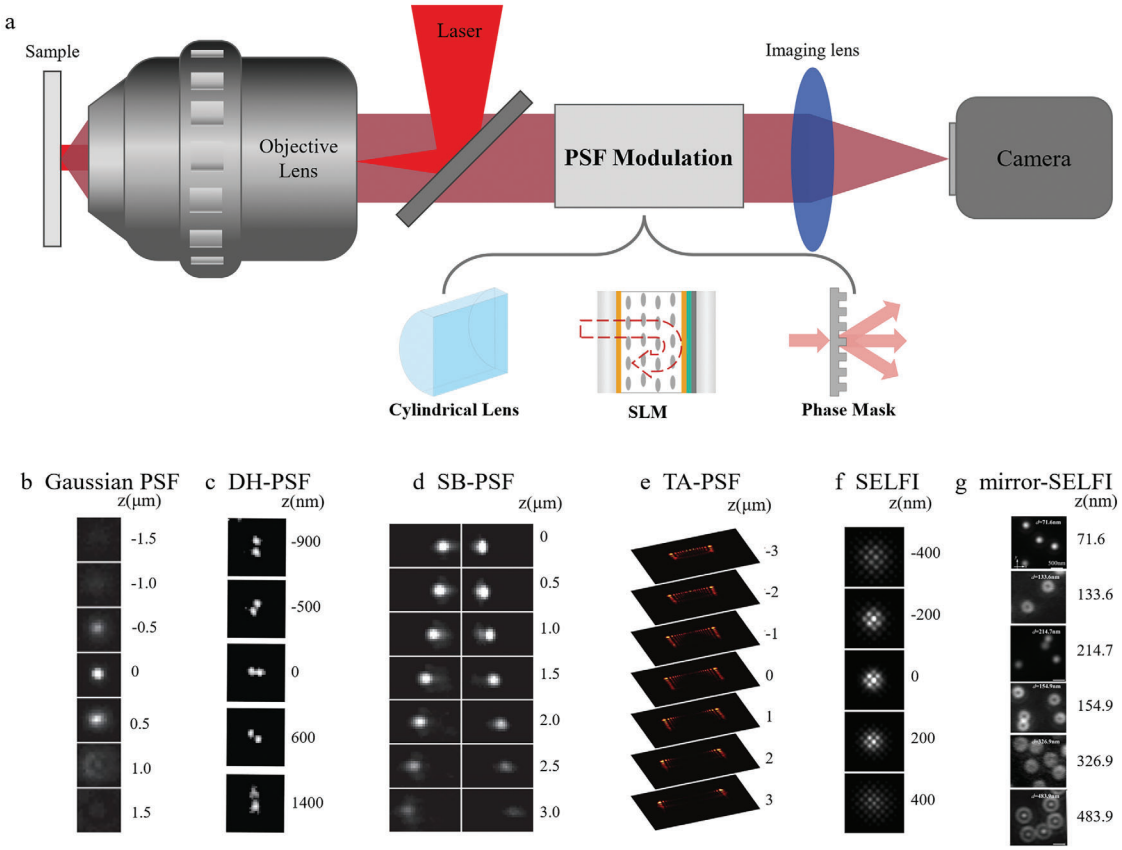

Figure 5. a) The optical path diagram for axial super-resolution localization based on PSF engineering. b–g) The intensity distribution of the modulated PSF at different axial positions: b) Gaussian PSF;[13d] Reproduced (Adapted) with permission.[13d] Copyright 2014, Springer Nature. c) DH-PSF;[13j] Reproduced (Adapted) with permission.[13j] Copyright 2009, National Academy of Sciences. d) SB-PSF;[13d] Reproduced (Adapted) with permission.[13d] Copyright 2014, Springer Nature. e) TA-PSF;[13k] Reproduced (Adapted) with permission.[13k] Copyright 2020, American Physical Society. f) SELFI;[13g] Reproduced (Adapted) with permission.[13g] Copyright 2018, Springer Nature. g) mirror-SELFI.[13a] Reproduced (Adapted) with permission.[13a] Copyright 2021, Springer Nature.

experimentally verified the feasibility of 3D-STORM by imaging microtubules and lattice protein-coated pits in cells. The lateral resolution can reach ≈20–30 nm, and the axial resolution can reach ≈50–60 nm.

By introducing a weak cylindrical lens into the imaging path, 3D-STORM creates two slightly different focal planes in the x and y directions.[55] Therefore, the ellipticity and orientation of the fluorescence image change with its position in z. Using this feature, the z coordinates of the fluorophore can be determined by fitting the fluorescence image with a 2D elliptical Gaussian function to obtain x and y coordinates at different positions and their widths w_x and w_y.

Since the image width of 3D-STORM increases as the fluorophore moves away from the focal plane, its localization accuracy decreases as the absolute value of z increases, especially in the lateral dimension. Although the enhanced astigmatism will increase the sensitivity of the PSF change and increase the axial resolution, it will also introduce additional interference, which will reduce the signal-to-noise ratio of the imaging.[56] Therefore, the imaging range of 3D-STORM is usually limited to about 600 nm near the focal plane. When imaging thick samples, the imaging depth can be increased by scanning along the z-axis.[57] The dual-objective scheme is also applicable to astigmatic imaging, further enhancing 3D resolution (with lateral localization precision smaller than 10 nm and axial localization precision smaller than 20 nm). Additionally, this method improves the signal-to-noise ratio of imaging by collecting fluorescence signals twice.[58]

4.3. Self-Bending PSF

The Airy beam was first proposed and experimentally generated by Siviloglou et al.[59] in 2007. Since then, due to its unique properties, including self-accelerating, self-healing, and non-diffracting, the Airy beam has been widely concerned and studied in depth.[60]

In 2014, Jia et al.[13d] proposed an isotropic 3D super-resolution imaging technique with Self-Bending PSF (SB-PSF) based on the characteristics of Airy beam. Their side-lobe-free SB-PSF has non-diffracting and propagation-dependent lateral bending characteristics, which is very suitable for accurate 3D localization of molecules at large imaging depth. When the Airy beam propagates, the transverse displacement will occur, which will lead to

the bending of the optical path, so the axial position of the fluorescent molecule can be determined by the transverse displacement of the beam (Figure 5d). By introducing a cubic spatial phase into the detection path of the microscope and placing a SLM on the Fourier plane, the fluorescence emission of a single molecule can be converted into an Airy beam in principle.[59,61] In order to facilitate the accurate 3D localization of the radiation source, they introduced two improvements to the Airy beam: The first improvement was that they introduced additional phase modulation on the SLM to eliminate the large side flap of the Airy beam. The other was that they split the unpolarized fluorescence emission into two orthogonally polarized beams and rotate one of the polarizations so that both beams are properly polarized for SLM. This dual-beam design not only reduces photon losses induced by the SLM, but also allows the two beams to bend in opposite directions during propagation, decoupling the transverse position of the emitter from the propagation-induced transverse displacement of the beam. Finally, a calibration curve between the axial position z and the lateral bending distance of the observed bead image is generated. Using this method, they recorded STORM images of immunolabelled microtubules and mitochondria in mammalian cells, which captured microtubules and mitochondria that are completely undetectable in conventional images due to diffraction and allowed super-resolution imaging that maintained a highly isotropic 3D localization accuracy of 10–15 nm over a range of 3 μm without the need for any sample or focal plane scanning.

SB-PSF provides higher axial localization accuracy and larger imaging depth range. However, similar to DH-PSF, the photon utilization efficiency of this method is also low. This can be alleviated by using a continuous phase mask prepared by gray-scale lithography technology, or by combining double objective lens detection, using ultra-bright light to activate fluorophores, and other methods.[62] In addition, the relatively large area and larger imaging depth of SB-PSF result in lower imaging speed and localized fluorophore density, which places higher demands for the duty cycle (on-off time ratio) of the optical switch probe.[63]

4.4. Twin Airy PSF

In order to extend the imaging depth of axial localization technology, Shechtman et al.[64] designed a set of tetrapod PSFs based on the information maximization framework and obtained the single fluorophore localization ability in the axial range of 7 μm. The lateral and axial localization accuracy is 12 and 21 nm, respectively. However, the phase recovery based maximum likelihood estimation [65] is required for the localization of the tetrapod PSF, which is computationally intensive, especially when the global optimization is used to avoid the local minimum of the likelihood function. In addition, in order to maintain the localization accuracy, the tetrapod PSFs are only suitable for imaging sparse samples. Based on this, Zhou et al.[13k] reported a super-resolution 3D localization method based on twin Airy beams in 2020. This method can produce accurate 3D localization and has the key advantages of expanding imaging depth range, high luminous flux and higher emission density imaging potential. In order to obtain the twin Airy beams, they designed a refractive phase mask for the twin Airy beams based on the pupil function,[13j,66] which will generate a PSF composed of two adjacent Airy beam lobes, and eventually generate a double image of each point separated from each other as the depth changes on the camera, which makes it possible to restore the axial position within the extended depth range of the Airy beam (Figure 5e). Among them, the use of refractive mask greatly simplifies the optical path, reduces the difficulty of imaging operation, and obtains 100% broadband luminous flux. Compared with the single Airy beam method, the Twin Airy PSF (TA-PSF) has a consistent sensitivity to defocus over the entire depth range, thus providing an effective axial localization range more than twice that of the single Airy beam method. In this work, they achieve a 3D localization accuracy better than 30 nm in a depth range of more than 7 μm.

4.5. Self-interference Fluorescence Microscope

In 2018, Bon et al.[13g] proposed a self-interference fluorescence microscope (SELFI) capable of deep-tissue 3D single-molecule localization with imaging depths up to 50 μm. SELFI generates PSF replicas with spatial overlap greater than 90% by inserting a pure phase-only diffraction grating of several microns in front of the microscope imaging plane to achieve self-interference. The interference pattern of the self-interference PSF at different defocus amounts varies with the axial position of the emitter (Figure 5f), and the envelope of the interference pattern directly corresponds to the microscope PSF without diffraction grating. Therefore, two independent variables can be obtained in one image, including wavefront curvature and intensity distribution within the envelope. Based on the dependence of the intensity and phase on the defocusing distance, they were able to extract the 3D position of the radiation source from the interferogram with sub-wavelength accuracy. The self-interference of PSF does not cause the lateral expansion of PSF. In 2019, Linarès-Loyez[67] also of Bon 's team, proved that SELFI can achieve 3D super-resolution imaging and 3D single-particle tracking of living cell samples, and its 3D localization depth can reach tens of microns. Furthermore, SELFI basically covers the most popular single-molecule imaging techniques for living cell samples, including PAINT,[68] PALM,[4f] SPT,[69] etc. As long as a single-molecule image can be formed on the imaging plane of the microscope, even for conventional surface-based fluorescence microscopes, SELFI can also achieve 3D localization beyond the diffraction limit by simultaneously measuring the intensity and phase of fluorescence. This opens new possibilities for the clear study of molecular nanostructures and dynamics in complex samples. However, the extraction of sub-wavelength precision 3D positions based on intensity and phase makes SELFI sensitive to the focal position, and any drift in the focus can easily affect the localization accuracy.

In 2021, Liu et al.[13a] proposed a self-interference fluorescence nanoparticle axial localization and tracking method based on the transverse PSF. This technology can simultaneously realize the lateral and axial super-resolution localization of nanoparticles in a frame of wide-field image, which solves the problem that the resolution anisotropy of the existing single-molecule localization technology and the optical localization method are greatly affected by defocus. The localization accuracy of real-time distance sensing can reach 2.8 nm. Therefore, this method can track rapidly moving biomolecules in live cells or biological

organs. This method is based on the confocal wide-field fluorescence system, and the upconversion nanoparticles are placed on a series of silica layer mirror substrates with characteristic thickness to realize the self-interference process of fluorescence. The axial position information of the nanoparticles is encoded into the far-field PSF pattern. By extracting PSF eigenvalues at different feature positions and establishing evaluation functions, 3D super-resolution positioning in wide-field images can be realized (Figure 5g). For the working range of this method, when the nanoparticles are farther than 500 nm from the mirror, the reflected emission intensity becomes too weak for SELFI, limiting its maximum working range to 500 nm. On the other hand, when the nanoparticles are too close to the mirror (less than 30 nm), the emission is affected by the quenching effect of the noble metal surface, resulting in a reduced signal-to-noise ratio and a decrease in localization resolution.

5. Encoding Axial Information into Alternative Dimensions

5.1. Encoding Axial Information into the Fluorescence Lifetime

FÖrster resonance energy transfer (FRET) is an electromagnetic field-mediated energy transfer process from a photoexcited donor to an acceptor. A fluorescent molecule (donor) is in an excited state by absorbing excitation light, and when it is in close proximity to another neighboring fluorescent molecule (acceptor), energy is transferred from the donor to the acceptor in a non-radiative form, and the donor's excited state must overlap with the acceptor's absorbed state. This process requires the distance between two molecules to be less than tens of nanometers, and its transfer efficiency depends on the sixth power of the distance between the donor and the acceptor (**Figure 6**a). Moreover, the fluorescence lifetime of a donor fluorophore changes when it undergoes FRET with an acceptor molecule. Specifically, the quenching of the donor emission by FRET leads to a decrease in its lifetime. The discovery of FRET has completely changed the ability of fluorescence imaging to measure intermolecular and intramolecular distances at the nanoscale.[70]

Based on this, in 2014, Chizhik et al.[71] proposed a living cell nanoscopy based on metal-induced energy transfer (MIET). This method replaces the acceptor molecule in FRET with a metal film to solve the molecular orientation problem of FRET (Figure 6b), and uses the measured energy transfer efficiency from the donor molecule to the metal surface plasmon to accurately infer the distance between the molecule and the metal,[72] which makes it possible to locate the fluorescent molecule with nanometer accuracy, and the distance range of effective energy transfer is an order of magnitude larger than that of traditional FRET. Specifically, MIET is based on a conventional FLIM system (Figure 6d), where a semi-transparent 20 nm gold film is deposited on the cover glass supporting the sample. Due to the planar geometry of the metal film as the acceptor, the distance dependence of energy transfer efficiency is much weaker than the sixth power of the distance. This results in a monotonic relationship between lifetime and distance in the range of 100–200 nm above the surface (Figure 6e). However, only using the fluorescence lifetime image cannot identify the area without cells, it is necessary to combine the fluorescence intensity image to identify the background area, and finally obtain the 3D reconstruction image of the cell basement membrane in the experiment. In addition, using a Fluorescence lifetime imaging microscopy (FLIM) based on a time-gated camera or a phase fluorescence method,[73] the acquisition speed can be increased by several orders of magnitude, thereby enabling dynamic image acquisition with high time resolution. MIET has a lateral resolution of 200 nm (defined by a confocal microscope) and an axial resolution of up to 3 nm. Combining it with optical switch-based super-resolution microscopy and single-molecule high-precision localization, nano-level 3D localization accuracy will be obtained.[74] In 2019, Ghosh et al.[13b] replaced the metal layer with graphene (Figure 6c),[75] which improved the localization accuracy of MIET by 10 times and called this method gMIET. Similar to metal-based MIET, fluorescence emission can be effectively coupled to graphene through distance-dependent electromagnetic near-field coupling, and its coupling range is about one order of magnitude smaller than that of metal (Figure 6f). Therefore, the axial resolution of gMIET is improved by 10 times, and sub-nanometer axial localization accuracy is obtained. In addition, the excellent optical transparency of graphene makes gMIET a very effective tool in single molecule research with limited photon budget. However, the imaging depth of both MIET and gMIET is limited by the coupling range, where MIET is about 200 nm and gMIET is about 20 nm, so the technology requires that the sample must be very close to the substrate surface.

5.2. Encoding Axial Information into Spectra

High-precision axial localization can also be obtained by encoding axial information into changes in the spectrum. In 2012, Groot et al.[76] proposed a 3D fluorescence imaging microscopy technique without axial scanning: self-interference fluorescence imaging (SIFM), which expands the ability of confocal microscopy by providing a depth sensitivity far superior to the axial spot size. The schematic diagram is shown in **Figure 7**a. The interference caused by the optical path difference between the light of the thicker outer ring of the phase plate and the light passing through the center hole realizes the modulation of the fluorescence spectrum. The solid red line in Figure 7a represents the wavefront of the light. The flat wavefront of the light source at the focus ($\delta = 0$ μm) and the curved wavefront of the light source at the defocus ($\delta = 100$ μm) introduce an additional path length difference $\Delta(\delta)$ and self-interference spectral phase shift. Therefore, the spectral phase directly encodes the axial position of the fluorescence source.

The lateral resolution in SIFM is determined by the NA of the objective lens and the aperture size of the fiber core, similar to confocal microscopy imaging, while the axial localization accuracy depends on the NA of the objective lens and the signal-to-noise ratio of the system. Therefore, simply collecting more photons or choosing an objective with a higher NA will result in higher localization accuracy, but at the expense of imaging depth.[78] Finally, in the depth range of 500 μm, SIFM can obtain the axial localization accuracy better than 4 μm by decoding the spectral phase information. In the high numerical aperture structure with small depth of field, the axial localization accuracy

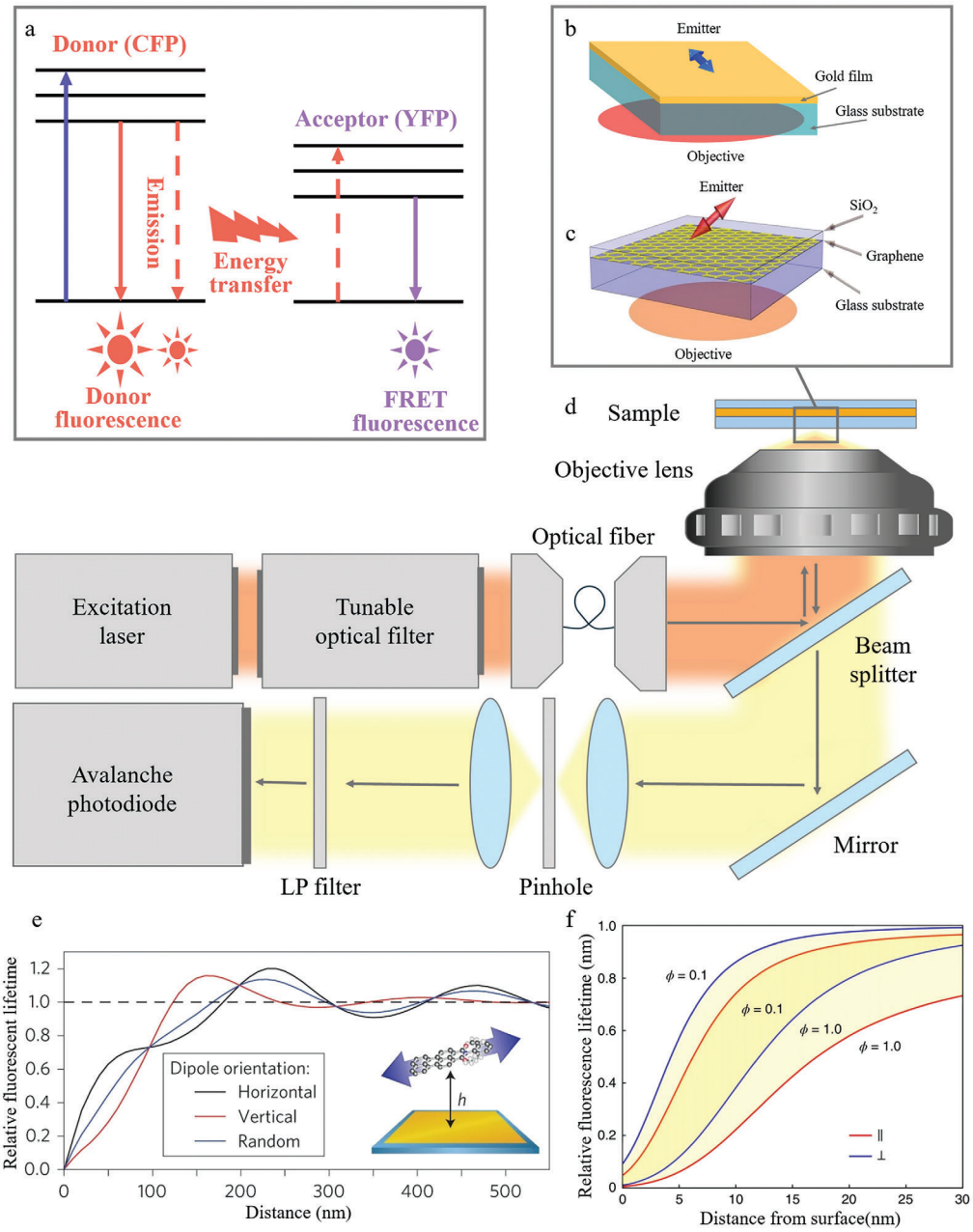

Figure 6. Principles of microscopes based on fluorescence lifetime information encoding. a) Principle of FRET. b) The sample composition of MIET. c) The sample composition of gMIET.[13b] Reproduced (Adapted) with permission.[13b] Copyright 2019, Spring Nature. d) Scheme of the experimental set-up. e) Dependence of the fluorophore lifetime on its axial position on the metal film (emission wavelength 650 nm, gold film thickness 20 nm).[71] Reproduced (Adapted) with permission.[71] Copyright 2014, Spring Nature. f) The relationship between relative fluorescence lifetime and surface distance. The blue and red curves represent the molecules perpendicular and parallel to the surface direction, respectively. The color region covers the quantum yield values between $\varphi = 0.1$ and $\varphi = 1.0$.[13b] Reproduced (Adapted) with permission.[13b] Copyright 2019, Spring Nature.

can reach tens of nanometers. However, the method is only good for sparse samples because of the light intensity-weighted average depth that is obtained in the case of multiple fluorescence sources.

In addition, in 2008, Mock et al.[77] proposed a method for axial localization based on the dependence of the plasmon resonance coupling between gold nanoparticles and metal films on the distance(Figure 7b,c). They placed gold nanoparticles far above the nanoscale of the metal film substrate, precisely controlled the spacing between the two by means of polyelectrolyte layers of different thicknesses and obtained scattering spectra and images of individual nanoparticles using dark-field microscopy and TIR illumination. A distance-dependent spectral profile was obtained using the coupling effect between the localized surface plasmon (LSP) generated by the resonance of the isolated excitons on the nanoparticles and the surface plasmon polaritons (SPP)

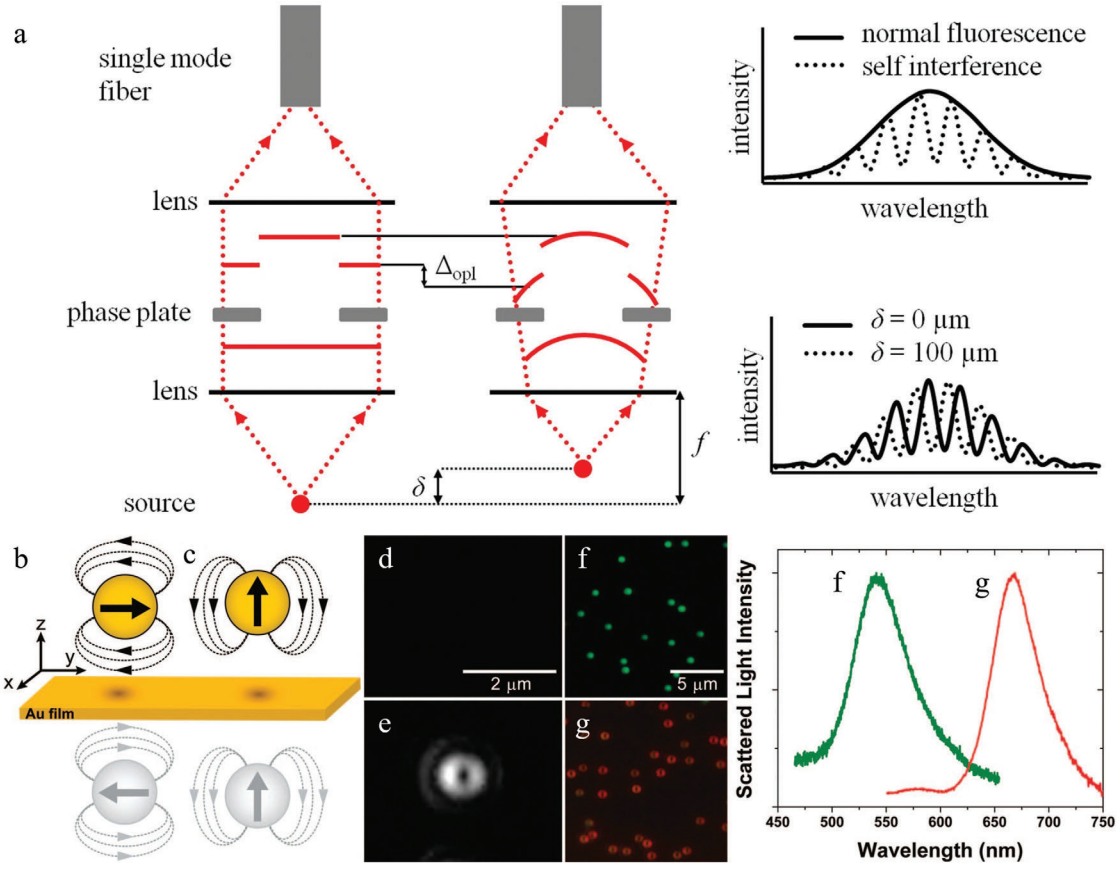

Figure 7. Principles of microscopes based on spectral information encoding. a) The schematic diagram of SIFM microscope.[76] Reproduced (Adapted) with permission.[76] Copyright 2012, Optical Society of America. b) Simplified representation of a plasmonic NP interaction with a gold film. The dipole parallel to the gold film is canceled out by the induced image dipole.[77] c) The dipole perpendicular to the gold film resonantly couples to the induced image dipole, is red shifted, and scatters asymmetrically.[77] d) Experimentally observed far-field scattering from a 60 nm gold NP on a 45 nm gold film illuminated with polarization parallel to the film (scattering is damped and is virtually undetectable).[77] e) The same NP as that in (d) but with a component of the illumination polarized perpendicular to the film, which couples to the vertically oriented dipole and is scattered into the far-field.[77] f) Color image and typical spectrum of 60 nm gold NPs in a quasi-uniform dielectric and g) on the surface of the 45 nm thick planar gold film (under dark-field illumination).[77] Reproduced (Adapted) with permission.[77] Copyright 2008, American Chemical Society.

generated by the polarizers of the isolated excitons on the gold film. The LSP resonance wavelength of the nanoparticles is blue shifted with increasing distance.[79] And, when the polarization of the incident light is partially perpendicular to the gold film, the scattering from the nanoparticles goes into the far field producing a donut-shaped PSF (Figure 7d,e). The shape and intensity of this PSF is very sensitive to the distance between the nanoparticles and the gold film and can also be used to accurately measure the change in distance between the two (Figure 7f,g). An axial localization accuracy of less than 1 nm can be obtained with this method, but the method has a number of limitations, including metal nanoparticles, metal substrates, and TIR illumination, and the coupling effect is most pronounced at distances less than 50 nm.

5.3. Encoding Axial Information into Optical Phase

The axial position information can also be encoded into the optical phase change. In 2021, Xu's research group and Ji's research group of the Institute of Biophysics, Chinese Academy of Sciences[13e] proposed an axially localized repetitive optical selective exposure (ROSE-Z) super-resolution imaging method based on interference fringes. The theoretical localization accuracy of ROSE-Z is (the interference fringe period is 263 nm):

$$\sigma \sim 263/2\pi\sqrt{N} \approx 42/\sqrt{N} \quad (5)$$

This method achieves axial localization accuracy of less than 2 nm with only about 3000 photons and achieves nanoscale 3D and two-color imaging. ROSE-Z obtains the axially excited interference fringes by dividing the laser beam into two parts and illuminating the sample from the opposite direction, as shown in **Figure** 8a. The imaging part of the optical path includes three ROSE detection optical paths, generating three sub-images corresponding to the three phases of the illumination mode (Figure 8b). Since the interferogram is periodic, additional astigmatism is introduced by a cylindrical mirror to provide initial axial information to determine the positional relationship between the axial localization of a single molecule and the

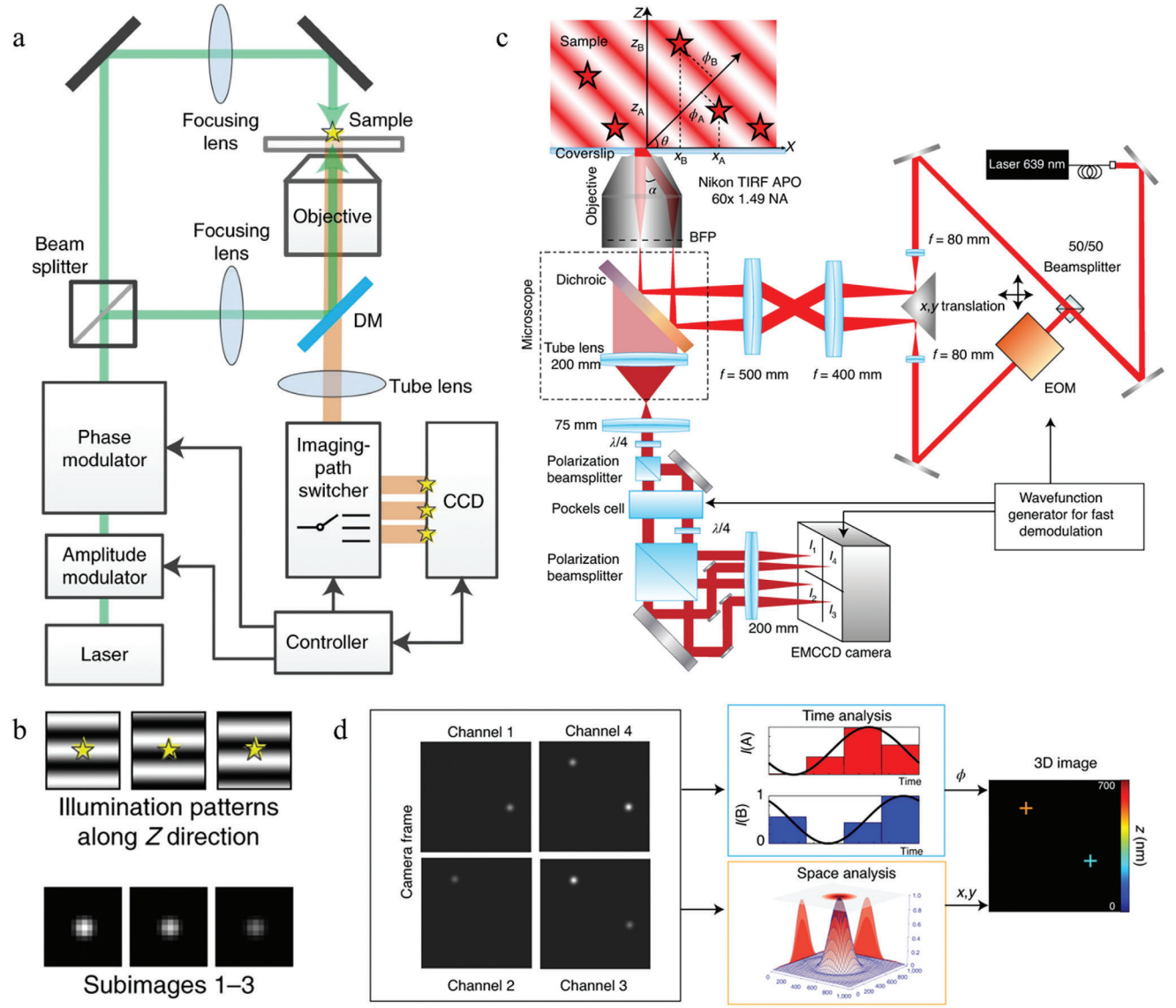

Figure 8. a) The light path diagram of ROSE-Z.[13e] b) The stripe lighting pattern along the *z* direction and the corresponding sub-images.[13e] Reproduced (Adapted) with permission.[13e] Copyright 2021, Springer Nature. c) Light path diagram of ModLoc.[13f] d) ModLoc axial localization is achieved by jointly analyzing the phase of the modulated fluorescence signal and the lateral localization information obtained through PSF standard centroid fitting.[13f] Reproduced (Adapted) with permission.[13f] Copyright 2021, Springer Nature.

periodic interference fringes, By combining the relationship between single-molecule axial localization and the periodic interference fringes, higher precision position information is obtained. Compared to other single-molecule localization methods with high axial resolution, ROSE-Z has the advantage of providing uniform resolution over the depth of field, as well as relative simplicity in design and ease of use. When combined with adaptive optics, it could further enhance imaging quality, enabling higher-resolution whole-cell volumetric imaging. However, its main disadvantage is the longer time required for localization.

Also in 2021, Jouchet et al.[13f] achieved single-molecule localization (ModLoc) using tilted interference fringes in combination with a fast demodulation scheme, achieving nanoscale localization accuracy up to 6.8 nm axially without affecting the acquisition time, emitter density, or lateral localization accuracy. Figure 8c shows the light path realization device of the ModLoc microscope. Lock-in detection is performed through four temporal channels. The phase is derived by measuring the intensity of fluorescence transmitted by each fluorophore to the channel. The axial localization is obtained by the joint analysis of the phase of the modulated fluorescence signal generated by the moving structured light and the lateral localization obtained by the PSF standard centroid fitting (Figure 8d).

The experimental data of ModLoc closely match the theoretical limit, achieving an axial localization precision of ≈7.4 nm. Both axial and lateral localization accuracies remain largely unchanged within a depth range of 7 µm. Compared to PSF-based techniques, this phase detection method is independent of PSF shape

Table 1. Summary of axial super-resolution imaging techniques.

Classification	Name	4Pi					
Localized Excitation	isoSTED	iPALM	4Pi-SMS	4Pi-RESOLFT	W-4PiSMSN	4Pi-STORM	
	Best resolution	≈40–50 nm	About 20 nm	≈5.4–6.6 nm	30 nm	≈10–20 nm	≈2–3 nm
	Advantage	Isotropic Resolution. Non-Invasive Imaging. Non-switchable fluorophores	Sub-20 nm 3D resolution. Maintains molecular specificity. High photon efficiency	Sub-10 nm 3D resolution. High-speed imaging. Accurate imaging thickness up to 650 nm	Low light intensity. Strong optical sectioning capabilities	Sub-20 nm 3D resolution. Imaging depth up to 10 microns. Robustness	Sub-10 nm 3D resolution. Suitable for thick specimens. Low artifacts
	Disadvantage	Complexity of Setup. Requires fluorophores match the excitation and emission parameters	Complex optical setup. Imaging positioning depth is relatively high small (250 nm)	Complex optical setup. Slow imaging speed	Complex optical setup; Slow imaging speed. Background signal	Complex optical setup. Slow imaging speed	Complex optical setup. Slow imaging speed
	Name	TIRF			Supercritical Angle		
		SIMPLER	3D-SAFM	vSAF	DONALD	DAISY	
	Best resolution	10 nm	sub-15 nm	26.4 ± 8.4 nm	20 nm	15 nm	
	Advantage	Minimal photodamage. Robustness. Compatible with any 2D SMLM	Highly sensitive for surface imaging. Compatible with other super-resolution microscopy	Simple and robust setup. Applicable to various samples	Nearly isotropic 3D resolution. Can calculate the absolute axial position	Nearly isotropic 3D resolution. Extended depth imaging (1 um). Robustness	
	Disadvantage	Limited imaging depth. Photon count dependence	Depth imaging resolution is limited. High data processing requirements: Stable fluorescence signal required	Limited axial range. Dependence on fluorophore rotation. Complex data processing	Most effective within a 150 nm range only. SNR dependence. Complex data processing	SNR dependence. Complex data processing. Photon loss	
Optical Frequency Shifting	Name	3D-SIM	I^5S	3D-SIM (two objective)	4-beam SIM		
	Best resolution	265 nm	80 nm	125 nm	Physical Method:160 nm Computational Method:120 nm		
	Advantage	Double resolution. Effectively removes out-of-focus blur. Efficient light use. Suitable for moderately thick samples	Near-Isotropic Resolution. Efficient light use. Suitable for moderately thick samples	Isotropic 3D resolution. Simplifying the experimental setup. Can be easily added to existing 3D-SIM microscopes	Physical Method: Achieving near-isotropic imaging. Minimal modification to the optical system. Computational Method. Isotropic resolution. Does not require hardware modifications		
	Disadvantage	Requires precise alignment; Slow imaging speed; Large amounts of computation	Requires precise alignment. Slow imaging speed. Large amounts of computation. Requires samples to be thin and optically homogeneous enough. Requires samples to be thin and optically homogeneous	Requires precise alignment and calibration. Requirement for specific objectives	Physical Method: Have ring artifacts in thicker samples. Computational Method: Requires significant data and time. Poor generalization ability		

(*Continued*)

Table 1. (Continued)

Classification	Name	4Pi					
Alternative Dimensions	Name	Fluorescence lifetime		Spectra		Optical Phase	
		MIET	gMIET	SIFM	Plasmon Resonance Coupling	ROSE-Z	ModLoc
	Best resolution	3 nm	Less than 1 nanometer	tens of nanometers	Less than 1 nanometer	Less than 2 nanometers	6.8 nm
	Advantage	High axial precision. Reduced orientation dependency compared to FRET.	High axial precision. Photon efficiency. Reduced orientation dependency.	No depth scanning required. Large depth-of-field (500 um).	High sensitivity. Real-time measurement	Minimal photon requirement. Simple Setup.	Deep imaging capability. Robustness to aberrations.
	Disadvantage	Limited to metal-coated substrates. Limited imaging range(100 nm). Lateral resolution has not improved much	Limited to graphene substrates. Surface roughness sensitivity. Limited imaging range(30nm)	Limited by sample density. Photon dependency	Limited to specific materials. Environmental sensitivity	Complex calibration. Computationally intensive	Complex calibration. Sensitivity to motion. Samples requiring long fluorescence lifetime
PSF Engineering	Name	DH-PSF	DH-PSF+STED	DH-PSF+light sheet	DH-PSF+MSIM	3D-STORM	
	Best resolution	30 nm	25 nm	30 nm	100 nm	≈50–60 nm	
	Advantage	Large depth of field. Compatible with existing wide-field microscopy systems	Can be integrated with existing STED microscopy systems	High contrast. Large depth of field. Real-time imaging	Rapid imaging. Large depth of field. Excellent compatibility. Low phototoxicity	No sample scanning. High photoswitch efficiency	
	Disadvantage	Signal loss. Sophisticated computational methods. Background noise	Signal loss. System complexity. Background noise	Signal loss. System complexity. Data processing demands	Signal loss due to phase mask. Data processing demands	High excitation source requirement. Resolution deteriorates with depth	
	Name	3D-STORM+two objective	SB-PSF	Tetrapod PSF	TA-PSF	SELFI	Self-interference fluorescence axial localization
	Best resolution	Less than 20 nm	≈10–15 nm	21 nm	Less than 30 nm	24 nm	2.8 nm
	Advantage	High photon utilization efficiency. Improved SNR. High mechanical stability	Large imaging depth(3um). Isotropic imaging	Large axial range. Scan-free tracking. Multiple particle tracking	Large axial range. Higher optical throughput. Simple Calibration	Deep tissue imaging. Less sensitivity to aberrations. Can be used for various biological samples	High axial precision. Real-time sensing. Widefield imaging compatibility. Defocus immunity
	Disadvantage	Complex optical setup. Long imaging time	Photon loss. Slower imaging speed	Huge amount of computation. Photon loss	High numerical aperture objectives are needed; Computational complexity	Limited by photon count. Computational intensity	Limited working range. Sample limitations

and exhibits strong robustness to optical aberrations. Therefore, ModLoc is particularly suitable for deep imaging of biological samples. Furthermore, ModLoc, when combined with a dual-objective configuration, further enhances localization precision. By incorporating multiplexing strategies, it enables multi-color imaging, and when coupled with fluorescence lifetime measurements, it allows for multi-directional localization or provides additional single-molecule level information. It is noteworthy that, to avoid phase wrapping, the axial projection of the fringe frequency must be greater than or equal to the focusing depth, which limits the number of fluorescence molecules available for axial localization, thus slightly compromising the axial localization precision. Additionally, this method requires temporal sparsity, with the modulation period needing to be much shorter than the average fluorescence molecule lifetime to retrieve the phase of the majority of emitters. Moreover, the average fluorescence molecule lifetime must be much shorter than the camera exposure time, which limits the available fluorescent dyes.

6. Conclusion

This paper provides a comprehensive review of the research progress in axial super-resolution imaging techniques, as shown in **Table 1**. In addition to the four categories of methods discussed above, many other significant axial super-resolution imaging techniques were not introduced. For example, applying minimal fluorescence photon fluxes microscopy to the axial direction can achieve axial localization accuracy of 2–3 nm.[80] Improving the axial resolution of LSFM by scanning beams, such as two-photon scanning beams,[81] Airy beams,[82] Bessel beams,[83] and lattice light-sheet,[84] is another important approach. The introduction of cryo-electron microscopy imaging techniques has enabled fluorescence super-resolution microscopy to analyze the 3D structure of organelles and protein complexes in a near-native state, offering broad prospects for improving axial resolution.[85] Furthermore, combining existing methods with deep learning is an important development direction.[39a,87] Fei et al.[86] proposed a novel light-sheet super-resolution imaging strategy based on deep learning. This deep learning-based single-image super-resolution algorithm combines multi-stage diffraction-controlled ultra-thin achromatic light sheets with multi-stage cascading convolutional neural networks, providing a powerful new tool for fast, 3D, and long-term dynamic imaging of living cells. Additionally, Park et al.[87] proposed a deep learning-based unsupervised super-resolution technique, which is applicable to a wide range of somatic cell fluorescence imaging scenarios, enhancing axial resolution and recovering suppressed visual details while removing imaging artifacts. This provides a simple and effective approach to obtaining isotropic 3D fluorescence super-resolution images.

Inevitably, no axial super-resolution imaging method is perfect. When considering a specific application, the performance of different methods should be comprehensively evaluated. For example, compared with other super-resolution imaging techniques, optical frequency-shifting super-resolution imaging has the main advantages of fast imaging speed, high sample applicability, and low phototoxicity, making it particularly suitable for wide-field imaging of living cells. TIRFM or SAFM is ideal for observing the regions of interest on the sample surface, such as cell membranes. For 3D localization and tracking of individual particles, PSF-engineering-based methods are a good choice. If higher localization precision is required, MIET or gMIET can be considered, but the corresponding localization range will be limited. Therefore, for any given method, careful consideration should be given before its application. It is worth noting that we observed that many of the axial super-resolution methods discussed in this review are based on similar multimodal integration ideas. For example, axial resolution can be further improved by combining the existing methods with the dual-objective approach; the axial localization depth can be extended by integrating TIRF-based methods with astigmatic imaging schemes, and ROSE-Z similarly integrates astigmatic imaging to provide initial axial position information. Additionally, encoding changes in the PSF shape into axial position using different modulation methods, which allows the fluorescence intensity to carry additional positional information, is a fundamental concept for achieving axial super-resolution localization through PSF engineering. Therefore, optimizing the PSF shape to achieve a modulation PSF that is both related to axial position and more robust holds promise for further enhancing axial localization precision. Mirrors play an important role in many axial super-resolution imaging techniques and often simplify the optical path. Combining existing methods with deep learning algorithms for image reconstruction and denoising can often improve imaging speed and quality while reducing reliance on hardware. Furthermore, utilizing micro-nano fabrication technologies to develop high-performance optical elements, such as photon crystals capable of enhancing orbital angular momentum, could optimize existing techniques and improve imaging quality. These directions provide a promising outlook for the future development of axial super-resolution imaging technologies. We hope this review will help researchers focusing on axial super-resolution imaging techniques, providing a reference for future research directions and breakthroughs in this field, and fostering more innovative opportunities for frontier research in life sciences.

Acknowledgements

This work was supported by National Natural Science Foundation of China (62275125, 62275121, 12204239, 62175109), Fundamental Research Funds for the Central Universities (30922010313), Youth Foundation of Jiangsu Province (BK20220946), Fundamental Research Funds for the Central Universities (2023102001), and Open Research Fund of Jiangsu Key Laboratory of Spectral Imaging & Intelligent Sense (JSGP202201).

Conflict of Interest

The authors declare no conflict of interest.

Keywords

axial localization precision, axial resolution, axial super-resolution imaging, fluorescence super-resolution imaging microscope

Received: November 12, 2024
Revised: December 25, 2024
Published online:

[1] E. Abbe, *Arch. Mikrosk. Anat.* **1873**, *9*, 413.
[2] M. Born, E. Wolf, E. Hecht, *Phys. Today* **2000**, *53*, 77.
[3] L. Schermelleh, A. Ferrand, T. Huser, C. Eggeling, M. Sauer, O. Biehlmaier, G. P. C. Drummen, *Nat. Cell Biol.* **2019**, *21*, 72.
[4] a) W. E. Moerner, L. Kador, *Phys. Rev. Lett.* **1989**, *62*, 2535; b) S. W. Hell, J. Wichmann, *Opt. Lett.* **1994**, *19*, 780; c) E. Betzig, *Opt. Lett.* **1995**, *20*, 237; d) R. M. Dickson, A. B. Cubitt, R. Y. Tsien, W. E. Moerner, *Nature* **1997**, *388*, 355; e) P. Török, T. Wilson, *Opt. Commun.* **1997**, *137*, 127; f) E. Betzig, G. H. Patterson, R. Sougrat, O. W. Lindwasser, S. Olenych, J. S. Bonifacino, M. W. Davidson, J. Lippincott-Schwartz, H. F. Hess, *Science* **2006**, *313*, 1642; g) S. W. Hell, *Science* **2007**, *316*, 1153; h) L. Möckl, D. C. Lamb, C. Bräuchle, *Angew. Chem., Int. Ed.* **2014**, *53*, 13972.
[5] H. Deschout, F. C. Zanacchi, M. Mlodzianoski, A. Diaspro, J. Bewersdorf, S. T. Hess, K. Braeckmans, *Nat. Methods* **2014**, *11*, 253.
[6] a) E. Betzig, G. H. Patterson, R. Sougrat, O. W. Lindwasser, S. Olenych, J. S. Bonifacino, M. W. Davidson, J. Lippincott-Schwartz, H. F. Hess, *Science* **2006**, *313*, 1642; b) M. G. Gustafsson, *Proc. Natl.*

Acad. Sci. USA **2005**, *102*, 13081; c) S. T. Hess, T. P. Girirajan, M. D. Mason, *Biophys. J.* **2006**, *91*, 4258; d) M. J. Rust, M. Bates, X. Zhuang, *Nat. Methods* **2006**, *3*, 793.

[7] a) M. Minsky, *Scanning* **1988**, *10*, 128; b) D. K. Hamilton, T. Wilson, C. J. R. Sheppard, *J. Microsc.* **1984**, *4*, 551; c) W. B. Amos, J. G. White, *Biol. Cell* **2003**, *95*, 335.

[8] a) W. Denk, K. Svoboda, *Neuron* **1997**, *18*, 351; b) F. Helmchen, W. Denk, *Nat. Methods* **2005**, *2*, 932; c) K. Svoboda, R. Yasuda, *Neuron* **2006**, *50*, 823; d) W. Denk, J. H. Strickler, W. W. Webb, *Science* **1990**, *248*, 73.

[9] W. R. Zipfel, R. M. Williams, W. W. Webb, *Nat. Biotechnol.* **2003**, *21*, 1369.

[10] a) D. S. Richardson, J. W. Lichtman, *Cell* **2015**, *162*, 246; b) H. R. Ueda, A. Ertürk, K. Chung, V. Gradinaru, A. Chédotal, P. Tomancak, P. J. Keller, *Nat. Rev. Neurosci.* **2020**, *21*, 61.

[11] a) J. Huisken, J. Swoger, F. Del Bene, J. Wittbrodt, E. H. Stelzer, *Science (New York, N.Y.)* **2004** ,*305*, 1007; b) T. F. Holekamp, D. Turaga, T. E. Holy, *Neuron* **2008**, *57*, 661; c) P. J. Keller, A. D. Schmidt, J. Wittbrodt, E. H. Stelzer, *Science (New York, N.Y.)* **2008**, *322*, 1065; d) B.-C. Chen, W. R. Legant, K. Wang, L. Shao, D. E. Milkie, M. W. Davidson, C. Janetopoulos, X. S. Wu, J. A. Hammer, Z. Liu, B. P. English, Y. Mimori-Kiyosue, D. P. Romero, A. T. Ritter, J. Lippincott-Schwartz, L. Fritz-Laylin, R. D. Mullins, D. M. Mitchell, J. N. Bembenek, A.-C. Reymann, R. Böhme, S. W. Grill, J. T. Wang, G. Seydoux, U. S. Tulu, D. P. Kiehart, E. Betzig, *Science* **2014**, *346*, 1257998.

[12] L. Schermelleh, R. Heintzmann, H. Leonhardt, *J. Cell Biol.* **2010**, *190*, 165.

[13] a) Y. Liu, Z. Zhou, F. Wang, G. Kewes, S. Wen, S. Burger, M. E. Wakiani, P. Xi, J. Yang, X. Yang, O. Benson, D. Jin, *Nat. Commun.* **2021**, *12*, 2019; b) A. Ghosh, A. Sharma, A. I. Chizhik, S. Isbaner, D. Ruhlandt, R. Tsukanov, I. Gregor, N. Karedla, J. Enderlein, *Nat. Photonics* **2019**, *13*, 860; c) L. Shao, B. Isaac, S. Uzawa, D. A. Agard, J. W. Sedat, M. G. Gustafsson, *Biophys. J.* **2008**, *94*, 4971; d) S. Jia, J. C. Vaughan, X. Zhuang, *Nat. Photonics* **2014**, *8*, 302; e) L. Gu, Y. Li, S. Zhang, M. Zhou, Y. Xue, W. Li, T. Xu, W. Ji, *Nat. Methods* **2021**, *18*, 369; f) P. Jouchet, C. Cabriel, N. Bourg, M. Bardou, C. Poüs, E. Fort, S. Lévêque-Fort, *Nat. Photonics* **2021**, *15*, 297; g) P. Bon, J. Linares-Loyez, M. Feyeux, K. Alessandri, B. Lounis, P. Nassoy, L. Cognet, *Nat. Methods* **2018**, *15*, 449; h) M. G. Gustafsson, L. Shao, P. M. Carlton, C. J. Wang, I. N. Golubovskaya, W. Z. Cande, D. A. Agard, J. W. Sedat, *Biophys. J.* **2008**, *94*, 4957; i) X. Li, Y. Wu, Y. Su, I. Rey-Suarez, C. Matthaeus, T. B. Updegrove, Z. Wei, L. Zhang, H. Sasaki, Y. Li, M. Guo, J. P. Giannini, H. D. Vishwasrao, J. Chen, S. J. Lee, L. Shao, H. Liu, K. S. Ramamurthi, J. W. Taraska, A. Upadhyaya, P. La Riviere, H. Shroff, *Nat. Biotechnol.* **2023**, *41*, 1307; j) S. R. Pavani, M. A. Thompson, J. S. Biteen, S. J. Lord, N. Liu, R. J. Twieg, R. Piestun, W. E. Moerner, *Proc. Natl. Acad. Sci. USA* **2009**, *106*, 2995; k) Y. Zhou, P. Zammit, V. Zickus, J. M. Taylor, A. R. Harvey, *Phys. Rev. Lett.* **2020**, *124*, 198104.

[14] L. J. M. N. o. t. R. A. S. Rayleigh, **1880**, *40*, 254.

[15] S. W. Hell, M. Schrader, H. T. M. Van Der Voort, **1997**, *187*, 1.

[16] S. Hell, E. H. K. Stelzer, *Opt. Commun.* **1992**, *93*, 277.

[17] a) X. Hao, Y. Li, S. Fu, Y. Li, Y. Xu, C. Kuang, X. Liu, *Eng.* **2022**, *11*, 146; b) S. Hell, E. H. K. Stelzer, *J. Opt. Soc. Am. A* **1992**, *9*, 2159.

[18] M. Bates, J. Keller-Findeisen, A. Przybylski, A. Huper, T. Stephan, P. Ilgen, A. R. Cereceda Delgado, E. D'Este, A. Egner, S. Jakobs, S. J. Sahl, S. W. Hell, *Nat. Methods* **2022**, *19*, 603.

[19] R. Schmidt, C. A. Wurm, S. Jakobs, J. Engelhardt, A. Egner, S. W. Hell, *Nat. Methods* **2008**, *5*, 539.

[20] G. Shtengel, J. A. Galbraith, C. G. Galbraith, J. Lippincott-Schwartz, J. M. Gillette, S. Manley, R. Sougrat, C. M. Waterman, P. Kanchanawong, M. W. Davidson, R. D. Fetter, H. F. Hess, **2009**, *106*, 3125.

[21] D. Aquino, A. Schönle, C. Geisler, C. v. Middendorff, C. A. Wurm, Y. Okamura, T. Lang, S. W. Hell, A. Egner, *Nat. Methods* **2011**, *8*, 353.

[22] F. Huang, G. Sirinakis, E. S. Allgeyer, L. K. Schroeder, W. C. Duim, E. B. Kromann, T. Phan, F. E. Rivera-Molina, J. R. Myers, I. Irnov, M. Lessard, Y. Zhang, M. A. Handel, C. Jacobs-Wagner, C. P. Lusk, J. E. Rothman, D. Toomre, M. J. Booth, J. Bewersdorf, *Cell* **2016**, *166*, 1028.

[23] a) R. H. Dicke, *Phys. Rev.* **1953**, *89*, 472; b) E. J. Ambrose, *Nature* **1956**, *178*, 1194.

[24] a) E. J. Ambrose, *Exp. Cell Res.* **1961**, *8*, 54; b) W. Lukosz, *J. Opt. Soc. Am.* **1979**, *69*, 1495; c) W. Lukosz, R. E. Kunz, *J. Opt. Soc. Am.* **1977**, *67*, 1615.

[25] D. Axelrod, *J. Cell Biol.* **1981**, *89*, 141.

[26] a) F. Lanni, A. S. Waggoner, D. L. Taylor, *J. Cell Biol.* **1985**, *100*, 1091; b) E. H. Hellen, D. Axelrod, *Methods Cell Biol.* **1987**, *4*, 337; c) D. Axelrod, *Traffic* **2001**, *2*, 764; d) D. Toomre, D. J. Manstein, *Trends. Cell Biol.* **2001**, *11*, 298.

[27] A. M. Szalai, B. Siarry, J. Lukin, D. J. Williamson, N. Unsain, A. Caceres, M. Pilo-Pais, G. Acuna, D. Refojo, D. M. Owen, S. Simoncelli, F. D. Stefani, *Nat. Commun.* **2021**, *12*, 517.

[28] R. Jungmann, M. S. Avendano, J. B. Woehrstein, M. Dai, W. M. Shih, P. Yin, *Nat. Methods* **2014**, *11*, 313.

[29] C. M. Winterflood, T. Ruckstuhl, D. Verdes, S. Seeger, *Phys. Rev. Lett.* **2010**, *105*, 108103.

[30] C. Cabriel, N. Bourg, P. Jouchet, G. Dupuis, C. Leterrier, A. Baron, M. A. Badet-Denisot, B. Vauzeilles, E. Fort, S. Leveque-Fort, *Nat. Commun.* **2019**, *10*, 1980.

[31] E. H. Hellen, D. Axelrod, *J. Opt. Soc. Am. B* **1987**, *4*, 337.

[32] T. Ruckstuhl, D. Verdes, *Opt. Express* **2004**, *12*, 4246.

[33] a) A. Dasgupta, J. Deschamps, U. Matti, U. Hübner, J. Becker, S. Strauss, R. Jungmann, R. Heintzmann, J. Ries, *Nat. Commun.* **2021**, *12*, 1180; b) J. Deschamps, M. Mund, J. Ries, *Opt. Express* **2014**, *22*, 29081; c) M. Oheim, A. Salomon, M. Brunstein, *Biophys. J.* **2020**, *118*, 2339.

[34] N. Bourg, C. Mayet, G. Dupuis, T. Barroca, P. Bon, S. Lécart, E. Fort, S. Lévêque-Fort, *Nat. Photonics* **2015**, *9*, 587.

[35] a) M. Amjadian, S. M. Mostafavi, J. Chen, Z. Kavehvash, J. Zhu, L. Wang, *IEEE Trans. Med. Imaging* **2021**, *40*, 2197; b) X. Liu, J. Yu, F. Liu, Y. Liu, H. Guo, Y. H. Ye, *Opt. Lett.* **2024**, *49*, 105; c) A. Shayei, Z. Kavehvash, M. Shabany, *Appl. Opt.* **2017**, *56*, 4454.

[36] C. J. R. Sheppard, S. Roth, R. Heintzmann, M. Castello, G. Vicidomini, R. Chen, X. Chen, A. Diaspro, *Opt. Express* **2016**, *24*, 27280.

[37] M. G. Gustafsson, *J. Microsc.* **2000**, *198*, 82.

[38] a) J. T. Frohn, H. F. Knapp, A. Stemmer, *Opt. Lett.* **2001**, *26*, 828; b) M. Gustafsson, D. A. Agard, J. W. Sedat, in *Biomedical Optics*, **2000**, *198*, 82; c) J. T. Frohn, H. F. Knapp, A. Stemmer, *Proc. Natl. Acad. Sci. USA* **2000**, *97*, 7232; d) R. Heintzmann, C. Cremer, in *European Conference on Biomedical Optics*, https://doi.org/10.1117/12.336833.

[39] J. D. Manton, F. Strohl, R. Fiolka, C. F. Kaminski, E. J. Rees, *Biomed. Opt. Express* **2020**, *11*, 2098.

[40] P. P. Laissue, R. A. Alghamdi, P. Tomancak, E. G. Reynaud, H. Shroff, *Nat. Methods* **2017**, *14*, 657.

[41] L. Shao, P. Kner, E. H. Rego, M. G. L. Gustafsson, *Nat. Methods* **2011**, *8*, 1044.

[42] a) M. Weigert, U. Schmidt, T. Boothe, A. Müller, A. Dibrov, A. Jain, B. Wilhelm, D. Schmidt, C. Broaddus, S. Culley, M. Rocha-Martins, F. Segovia-Miranda, C. Norden, R. Henriques, M. Zerial, M. Solimena, J. Rink, P. Tomancak, L. Royer, F. Jug, E. W. Myers, *Nat. Methods* **2018**, *15*, 1090; b) M. Weigert, L. Royer, F. Jug, G. Myers, *in Medical Image Computing and Computer-Assisted Intervention – MICCAI 2017* (Eds: M. Descoteaux, L. Maier-Hein, A. Franz, P. Jannin, D. L. Collins, S. Duchesne), Springer International Publishing, Berlin **2017**.

[43] X. Liu, C. Kuang, X. Hao, C. Pang, P. Xu, H. Li, Y. Liu, C. Yu, Y. Xu, D. Nan, W. Shen, Y. Fang, L. He, X. Liu, Q. Yang, *Phys. Rev. Lett.* **2017**, *118*, 076101.

[44] a) S. Cao, T. Wang, Q. Sun, B. Hu, U. Levy, W. Yu, *Opt. Express* **2017**, *25*, 14494; b) S. Cao, T. Wang, J. Yang, B. Hu, U. Levy, W. Yu, *Sci. Rep.* **2017**, *7*, 1328.
[45] a) A. Bezryadina, J. Zhao, Y. Xia, X. Zhang, Z. Liu, *ACS Nano* **2018**, *12*, 8248; b) J. L. Ponsetto, A. Bezryadina, F. Wei, K. Onishi, H. Shen, E. Huang, L. Ferrari, Q. Ma, Y. Zou, Z. Liu, *ACS Nano* **2017**, *11*, 5344.
[46] a) S. Ekgasit, C. Thammacharoen, F. Yu, W. Knoll, *Anal. Chem.* **2004**, *76*, 2210; b) Z. Zhang, P. Ahn, B. Dong, O. Balogun, C. Sun, *Sci. Rep.* **2013**, *3*, 2803; c) A. Bezryadina, J. Zhao, Y. Xia, Y. U. Lee, X. Zhang, Z. Liu, *Opt. Lett.* **2019**, *44*, 2915; d) Z. Li, W. Kong, C. Wang, M. Pu, Y. Luo, X. Liu, W. Du, X. Ma, X. Li, X. Luo, *J. Phys. D: Appl. Phys.* **2021**, *54*, 215101; e) S. Kawata, Y. Inouye, P. Verma, *Nat. Photonics* **2009**, *3*, 388.
[47] D. S. Chaudhuri, D. A. N. Rajagopalan, in Springer, New York, https://doi.org/10.1007/978-1-4612-1490-8.
[48] A. Greengard, Y. Y. Schechner, R. Piestun, *Opt. Lett.* **2006**, *31*, 181.
[49] a) M. O. Lenz, H. G. Sinclair, A. Savell, J. H. Clegg, A. C. Brown, D. M. Davis, C. Dunsby, M. A. Neil, P. M. French, *J. Biophotonics* **2014**, *7*, 29; b) T. J. Gould, D. Burke, J. Bewersdorf, M. J. Booth, *Opt. Express* **2012**, *20*, 20998.
[50] S. R. P. Pavani, R. Piestun, *Opt. Express* **2008**, *16*, 3484.
[51] H. L. Lee, S. J. Sahl, M. D. Lew, W. E. Moerner, *Appl. Phys. Lett.* **2012**, *100*, 153701.
[52] S. R. Pavani, R. Piestun, *Opt. Express* **2008**, *16*, 22048.
[53] a) Y. Shechtman, S. J. Sahl, A. S. Backer, W. E. J. P. r. l. Moerner, *Phys. Rev. Lett.* **2014**, *113 13*, 133902; b) K. I. Mortensen, L. S. Churchman, J. A. Spudich, H. Flyvbjerg, *Nat. Methods* **2010**, *7*, 377; c) A. Gahlmann, J. L. Ptacin, G. Grover, S. Quirin, L. von Diezmann, M. K. Lee, M. P. Backlund, L. Shapiro, R. Piestun, W. E. Moerner, *Nano Lett.* **2013**, *13*, 987; d) J. Yoon, C. J. Comerci, L. E. Weiss, L. Milenkovic, T. Stearns, W. E. Moerner, *Biophys. J.* **2019**, *116*, 319; e) A. Agrawal, W. Colomb, S. Gaumer, *Microsc. Microanal.* **2020**, *26*, 1586.
[54] B. Huang, W. Wang, M. Bates, X. Zhuang, *Science (New York, N.Y.)* **2008**, *319*, 810.
[55] a) L. Holtzer, T. Meckel, T. J. A. P. L. Schmidt, **2007**, *90*, 053902; b) H. P. Kao, A. S. Verkman, *Biophys. J.* **1994**, *67*, 1291.
[56] a) I. Izeddin, M. El Beheiry, J. Andilla, D. Ciepielewski, X. Darzacq, M. Dahan, *Opt. Express* **2012**, *20*, 4957; b) B. Huang, W. Wang, M. Bates, X. Zhuang, *Appl. Phys. Lett.* **2008**, *319*, 810; c) S. Hell, G. Reiner, C. Cremer, E. H. K. Stelzer, *J. Microsc.* **1993**, *169*, 391.
[57] B. Huang, S. A. Jones, B. Brandenburg, X. Zhuang, *Nat. Methods* **2008**, *5*, 1047.
[58] K. Xu, H. P. Babcock, X. Zhuang, *Nat. Methods* **2012**, *9*, 185.
[59] G. A. Siviloglou, J. Broky, A. Dogariu, D. N. Christodoulides, *Phys. Rev. Lett.* **2007**, *99*, 213901.
[60] a) Y. Zhou, V. Zickus, P. Zammit, J. M. Taylor, A. R. Harvey, *Biomed. Opt. Express* **2018**, *9*, 6444; b) P. Zammit, A. R. Harvey, G. Carles, in *Imaging and Applied Optics*, Optica Publishing Group, CT2E.2, Arlington **2015**; c) P. Polynkin, M. Kolesik, J. V. Moloney, G. A. Siviloglou, D. N. Christodoulides, *Science (New York, N.Y.)* **2009**, *324*, 229.
[61] G. A. Siviloglou, D. N. Christodoulides, *Opt. Lett.* **2007**, *32*, 979.
[62] a) G. Grover, S. Quirin, C. Fiedler, R. Piestun, *Biomed. Opt. Express* **2011**, *2*, 3010; b) J. C. Vaughan, S. Jia, X. Zhuang, *Nat. Methods* **2012**, *9*, 1181.
[63] G. T. Dempsey, J. C. Vaughan, K. H. Chen, M. Bates, X. Zhuang, *Nat. Methods* **2011**, *8*, 1027.
[64] a) Y. Shechtman, S. J. Sahl, A. S. Backer, W. E. Moerner, *Phys. Rev. Lett.* **2014**, *113*, 133902; b) Y. Shechtman, L. E. Weiss, A. S. Backer, S. J. Sahl, W. E. Moerner, *Nano Lett.* **2015**, *15*, 4194.
[65] R. J. Ober, S. Ram, E. S. Ward, *Biophys. J.* **2004**, *86*, 1185.
[66] Y. Zhou, M. Handley, G. Carles, A. R. J. A. P. Harvey, *APL Photonics* **2019**, *4*, 050401.
[67] J. Linarès-Loyez, J. S. Ferreira, O. Rossier, B. Lounis, G. Giannone, L. Groc, L. Cognet, P. Bon, *Front. Phys.* **2019**, *7*, 00068.
[68] A. Sharonov, R. M. Hochstrasser, *Proc. Natl. Acad. Sci. USA* **2006**, *103*, 18911.
[69] S. Manley, J. M. Gillette, G. H. Patterson, H. Shroff, H. F. Hess, E. Betzig, J. Lippincott-Schwartz, *Nat. Methods* **2008**, *5*, 155.
[70] a) T. J. A. d. P. *Förster Resonance Energy Transfer*, Springer, Berlin **1948**; b) L. Stryer, R. P. Haugland, *Proc. Natl. Acad. Sci. USA* **1967**, *58*, 719; c) R. M. Clegg, *Methods Enzymol.* **1992**, *211*, 353; d) P. R. Selvin, *Methods Enzymol.* **1995**, *246*, 300.
[71] A. I. Chizhik, J. Rother, I. Gregor, A. Janshoff, J. Enderlein, *Nat. Photonics* **2014**, *8*, 124.
[72] K. H. Drexhage, *Progress in Opics*, Elsevier, Amsterdam **1974**.
[73] a) T. W. J. Gadella, T. M. Jovin, R. M. Clegg, *Biophys. Chem.* **1993**, *48*, 221; b) R. Datta, T. M. Heaster, J. T. Sharick, A. A. Gillette, M. C. Skala, *J. Biomed. Opt.* **2020**, *25*, 071203.
[74] N. Karedla, A. M. Chizhik, S. C. Stein, D. Ruhlandt, I. Gregor, A. I. Chizhik, J. Enderlein, *J. Chem. Phys.* **2018**, *148*, 204201.
[75] J. W. Weber, V. E. Calado, M. C. M. van de Sanden, *Appl. Phys. Lett.* **2010**, *97*, 091904.
[76] M. de Groot, C. L. Evans, J. F. de Boer, *Opt. Express* **2012**, *20*, 15253.
[77] J. J. Mock, R. T. Hill, A. Degiron, S. Zauscher, A. Chilkoti, D. R. Smith, *Nano Lett.* **2008**, *8*, 2245.
[78] F. Huang, T. M. Hartwich, F. E. Rivera-Molina, Y. Lin, W. C. Duim, J. J. Long, P. D. Uchil, J. R. Myers, M. A. Baird, W. Mothes, M. W. Davidson, D. Toomre, J. Bewersdorf, *Nat. Methods* **2013**, *10*, 653.
[79] R. R. Chance, A. Prock, R. Silbey, *Phys. Rev. A* **1975**, *12*, 1448.
[80] K. C. Gwosch, J. K. Pape, F. Balzarotti, P. Hoess, J. Ellenberg, J. Ries, S. W. Hell, *Nat. Methods* **2020**, *17*, 217.
[81] T. V. Truong, W. Supatto, D. S. Koos, J. M. Choi, S. E. Fraser, *Nat. Methods* **2011**, *8*, 757.
[82] T. Vettenburg, H. I. Dalgarno, J. Nylk, C. Coll-Lladó, D. E. Ferrier, T. Čižmár, F. J. Gunn-Moore, K. Dholakia, *Nat. Methods* **2014**, *11*, 541.
[83] T. A. Planchon, L. Gao, D. E. Milkie, M. W. Davidson, J. A. Galbraith, C. G. Galbraith, E. Betzig, *Nat. Methods* **2011**, *8*, 417.
[84] B. C. Chen, W. R. Legant, K. Wang, L. Shao, D. E. Milkie, M. W. Davidson, C. Janetopoulos, X. S. Wu, J. A. Hammer 3rd, Z. Liu, B. P. English, Y. Mimori-Kiyosue, D. P. Romero, A. T. Ritter, J. Lippincott-Schwartz, L. Fritz-Laylin, R. D. Mullins, D. M. Mitchell, J. N. Bembenek, A. C. Reymann, R. Böhme, S. W. Grill, J. T. Wang, G. Seydoux, U. S. Tulu, D. P. Kiehart, E. Betzig, *Science* **2014**, *346*, 1257998.
[85] a) F. K. Schur, *Curr. Opin. Struct. Biol.* **2019**, *58*, 1; b) Y.-W. Chang, S. Chen, E. I. Tocheva, A. Treuner-Lange, S. Löbach, L. Søgaard-Andersen, G. J. Jensen, *Nat. Methods* **2014**, *11*, 737; c) S. Weisenburger, D. Boening, B. Schomburg, K. Giller, S. Becker, C. Griesinger, V. Sandoghdar, *Nat. Methods* **2017**, *14*, 141; d) P. D. Dahlberg, W. E. Moerner, *Annu. Rev. Phys. Chem.* **2021**, *72*, 253; e) K. A. Sochacki, G. Shtengel, S. B. van Engelenburg, H. F. Hess, J. W. Taraska, *Nat. Methods* **2014**, *11*, 305.
[86] Y. Zhao, M. Zhang, W. Zhang, Y. Zhou, L. Chen, Q. Liu, P. Wang, R. Chen, X. Duan, F. Chen, H. Deng, Y. Wei, P. Fei, Y. H. Zhang, *Nat. Methods* **2022**, *19*, 359.
[87] H. Park, M. Na, B. Kim, S. Park, K. H. Kim, S. Chang, J. C. Ye, *Nat. Commun.* **2022**, *13*, 3297.

Qiwen Tan, a graduate student at Nanjing University of Science and Technology, is mainly engaged in the field of fluorescence super-resolution research.

Hongjun Wu, Lecturer at Nanjing University of Science and Technology, is engaged in fundamental and applied re- search in laser medicine, with a primary focus on the application of microscopic imaging in biomedicine.

Yongtao Liu, professor at Nanjing University of Science and Technology, is mainly engaged in modern super-resolution optical imaging, nanophotonics, nanosensing and characterization and related technologies in biomedical applications.

Qian Chen, professor at Nanjing University of Science and Technology, is engaged in the field of photoelectric detection and image processing research, focusing on ultra-high sensitivity ultra-fast photon imaging, fast 3D imaging and 3D microscopic imaging, mid-far infrared thermal imaging, color low-illumination imaging and other theories and technologies.

Chao Zuo, professor at Nanjing University of Science and Technology, is dedicated to the development of next-generation computational imaging and sensing technologies with a special emphasis on microscopy, metrology, biomedicine, human-computer interaction, and remote sensing.